ABSTRACT

HOLMAN, BRIAN SCOTT. A Study on the Merits of Using Computational Fluid Dynamics to Predict Thermal-Hydraulic Properties in Rod Bundles. (Under the direction of Dr. J. Michael Doster).

Subchannel methods are widely used in nuclear reactor thermal-hydraulic calculations. These methods rely heavily on empirical correlations, many of which were determined decades ago. Computational fluid dynamics (CFD) techniques rely less heavily on empirical correlations and are capable of much finer spatial resolution in rod bundle geometries. However, the computational requirements of using CFD for core wide thermal-hydraulic simulations is often impractical for most nuclear engineering applications, while subchannel codes can be deployed on machines with modest computing power and still achieve reasonable execution times. Given the practical advantages of subchannel methods, and the increased accuracy of CFD methods, of interest is the ability to use CFD methods to improve the accuracy of the subchannel predictions. The purpose of this work is to determine the validity of using CFD in lieu of experiments to "inform" the subchannel calculations by using CFD as a virtual experiment to update or replace the current empirical correlations. Of particular interest are those correlations used for turbulent mixing.

Sensitivity studies showed turbulent crossflow had a small effect on fluid enthalpy and flow, while heat transfer coefficient had an impact on wall temperature and the predicted height for the onset of nucleate boiling. These results provide an incentive to predict these terms with greater accuracy.

Three turbulent mixing experiments were reproduced using the CFD code ANSYS CFX. It was found that CFX made acceptable predictions for flow and thermal properties, but made poor predictions for mixing and turbulence for the simulated geometries when using a fine mesh. The turbulence kinetic energy was under predicted by an order of magnitude for this case. When using a coarse mesh, the turbulence characteristics were predicted more accurately. Further testing on the effects of different mesh sizes must be done with CFX to determine the best mesh size that would most accurately represent the thermal-hydraulic characteristics of the bundle. Other CFD codes should also be explored to assess their relative accuracy.

A Study on the Merits of Using Computational Fluid Dynamics to Predict Thermal-Hydraulic Properties in Rod Bundles

by
Brian Holman

A thesis submitted to the Graduate Faculty of
North Carolina State University
in partial fulfillment of the
requirements for the degree of
Master of Science

Nuclear Engineering

Raleigh, North Carolina

2012

APPROVED BY:

Dr. Hong Luo

Dr. Igor Bolotnov

Dr. J. Michael Doster
Chair of Advisory Committee

BIOGRAPHY

Brian Holman was born in New Orleans, LA, and graduated from Benjamin Franklin High School in 2006. He enrolled at North Carolina State University in the Nuclear Engineering program, which was the same program from which his father graduated many years ago. He completed his Bachelor's degree in 2010, and stayed for a Master's degree under the direction of Dr. J. Michael Doster. He worked on reactor thermal-hydraulics utilizing Computational Fluid Dynamics, and graduated in 2012.

ACKNOWLEDGMENTS

The author would like to thank Dr. J. Michael Doster for his guidance and invaluable advice on all aspects of this project leading to its successful completion. He would also like to thank Dr. Hong Luo for lending his expertise in the area of CFD to aid in the understanding of turbulence modeling and the interpretation of results. The author would also like to express gratitude to Dr. Igor Bolotnov for his engaging discussions on ways to better the CFD predictions. The author also thanks Dr. Cyrus Proctor for his introduction to and assistance in using ANSYS CFX, including mesh design. Additional thanks to Yidong Xia for providing his FLUENT results to be used as a comparison to the CFX and experimental results, and to Gary Howell for his time and effort devoted to troubleshooting issues with CFX on the NC State high performance computing system. Lastly, the author thanks the Consortium for Advanced Simulation of Light Water Reactors (CASL) for providing the necessary funding to support this research.

TABLE OF CONTENTS

LIST OF TABLES

LIST OF FIGURES

LIST OF SYMBOLS

Symbol	Description
A_i	Cross sectional area of subchannel i
ρ_i	Density of subchannel i
t	Time
u_i	Internal energy of subchannel i
h_i	Enthalpy of subchannel i
v_i	Velocity of subchannel i
$w_{i,j}$	Diversion crossflow from subchannel i to j
$w'_{i,j}$	Turbulent crossflow from subchannel i to j
g	Acceleration due to gravity
$S_{i,j}$	Rod gap between subchannel i and j
P_i	Pressure of subchannel i
Re	Reynolds number
D_e	Equivalent diameter

1 Introduction

1.1 Overview and Motivation for Research

Nuclear reactors are required to operate within specified thermal limits, which requires an accurate prediction of thermal-hydraulic parameters to ensure the design of these systems will be within acceptable margins. Subchannel analysis is a commonly used tool to predict thermal-hydraulic conditions in reactor fuel bundles. Subchannel methods have been used for many years, but rely heavily on correlations determined from experiments, many of which were performed decades ago. In some cases, these experiments were not performed under reactor-like conditions, but rather at atmospheric temperature and pressure or with lower flow rates and different geometry, which could introduce errors in the use of these correlations. Computational fluid dynamics (CFD) techniques rely less heavily on empirical correlations and are capable of much finer spatial resolution in rod bundle geometries. However, the computational requirements of using CFD for core wide thermal-hydraulic simulations is often impractical for most nuclear engineering applications, while subchannel codes can be deployed on machines with modest computing power and still achieve reasonable execution times. Subchannel analysis thus remains an attractive choice for simulating the thermal-hydraulic conditions in nuclear power systems.

Subchannel analysis is a pseudo three dimensional approach using area-averaged equations to predict thermal-hydraulic parameters in reactor fuel bundles. A subchannel is defined as the fluid area between a group of adjacent rods, as shown in Figure 1-1. Each subchannel is open to all other subchannels within a bundle, which allows crossflow between adjacent subchannels to occur. This crossflow transfers mass, energy, and momentum between the subchannels. Mixing in rod bundles is accomplished in two ways: pressure driven crossflow and turbulent crossflow. Pressure driven crossflows are the net flow from one subchannel to another due to lateral pressure differences between the subchannels. Turbulent mixing, or turbulent interchange, is the transfer of energy and momentum through eddies without net transfer of mass. It can play a significant role in the transfer of energy

from subchannel to subchannel in rod bundles, and thus has an effect on critical heat flux (CHF).

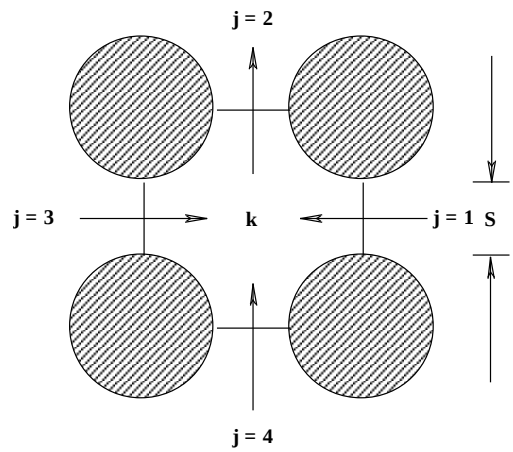

Figure 1-1. A subchannel for a square array rod bundle.

The subchannel equations can be derived in a variety of ways, but the formal approach is to average the Navier-Stokes equations over the cross sectional area of the subchannel. This approach provides conservation equations for area average fluid properties. Correlations are developed from empirical data produced by experiments for wall heat transfer rates, friction factors, turbulent crossflow, etc. The equations below are representative equations for the subchannel methods. The first is the mass conservation equation:

$$A_k \frac{\partial \rho_k}{\partial t} + \frac{\partial}{\partial z}\left(\rho_k v_k A_k\right) = \sum_j w_{j,k} \tag{1.1}$$

where z is the axial direction. The crossflow contribution is summed from each adjacent channel (see Figure 1-1). The energy conservation equation is formed by neglecting kinetic and potential energy terms, since they are very small in rod bundles, and is shown below:

$$A_k \frac{\partial \rho_k u_k}{\partial t} + \frac{\partial}{\partial z}(\rho_k h_k v_k A_k) - \sum_j w_{j,k} h^* - \sum_j w'_{j,k}\left(h_j - h_k\right) = \dot{q}'_k \tag{1.2}$$

where the second term denotes the axial flow, the third term is the pressure driven crossflow, the fourth term is the turbulent crossflow, and the last term is the wall heat transfer rate. The turbulent crossflow is determined from empirical correlations. The parameter h^* is the enthalpy convected across the gap from one subchannel to the other, and is taken to be the average enthalpy of the subchannel from which energy is convected. Two momentum conservation equations are needed, one for the axial momentum and one for the lateral momentum across each gap. The lateral momentum equation reflects differences in the conditions between subchannels that create lateral pressure gradients, leading to lateral crossflow between adjacent subchannels. The following is the axial momentum conservation equation:

$$A_k \frac{\partial \rho_k v_k}{\partial t} + \frac{\partial}{\partial z}(\rho_k v_k v_k A_k) - \sum_j w_{j,k} v^* - \sum_j w'_{j,k}(v_j - v_k) = -A_k \frac{\partial P_k}{\partial z} - (\tau_w P_w)_z - \rho_k A_k g \tag{1.3}$$

where v^* is the axial velocity of the subchannel from which momentum is transferred and g is the acceleration due to gravity. The convective terms are similar to those in the energy equation. The lateral momentum conservation equation is as follows:

$$l \frac{\partial w_{j,k}}{\partial t} + \frac{\partial}{\partial z}(w_{j,k} l v_z) = S_{j,k}(P_j - P_k) - (\tau_w P_w)_y \tag{1.4}$$

where l is the centroid distance between the subchannels. The presence of spacer grids adds resistance to flow in both the axial and lateral directions, as well as affecting the local flow parameters. A loss coefficient for the spacer grid can be found using a correlation based on the geometry of the grid [1], but the effect of the spacer grid on local flow parameters may not be adequately captured in the empirical data on which the subchannel methods rely.

Given the practical advantages of subchannel methods, and the increased accuracy of CFD methods, of interest is the ability to use CFD methods to improve the accuracy of the subchannel predictions. The purpose of this paper is to determine the merits of using CFD in lieu of experiments to “inform” the subchannel calculations by using CFD as a virtual experiment to update or replace the current empirical correlations. Of particular interest are

those correlations used for turbulent mixing. Using CFD would save time and money by substantially limiting the number of physical experiments, and it would allow CFD "experiments" to be performed under reactor conditions, thus leading to more applicable data.

1.2 Literature Review

Turbulent mixing plays a large role in the energy transfer within rod bundles. It is imperative to model this phenomenon as accurately as possible to preserve CHF margin and extract the most energy from the fuel as possible. Many experiments have been performed to learn more about turbulent mixing and its causes in rod bundles, as well as to correlate the data with respect to channel averaged properties.

Early experiments were performed to determine the turbulent flow structure in rod bundles and the cause of turbulent mixing. Rowe's [1] results revealed that the turbulence intensity is largest in the rod gap and smallest in the center of the subchannel. He noted that the rod gap spacing affected the flow of the fluid. Decreasing rod gap spacing led to increasing turbulence intensity due to increased secondary flows and flow pulsation frequency in the rod gap area. Both Rowe and Castellana [2] determined turbulent mixing was weakly dependent on axial Reynolds number. Rehme [3] concluded from studying others' work that secondary flow from subchannel to subchannel, the previously assumed driver of turbulent crossflow, is not large enough to cause meaningful changes in the mixing rate, and thus is not the source of turbulent mixing. These secondary flows are significant within each subchannel but do not traverse the channel affecting other subchannels to a large degree. The true cause of turbulent mixing was determined by Moeller [4]. He performed experiments on large scale eddy flow pulsations in rod bundles and determined that mixing caused by these flow pulsations was consistent with the literature and other mixing correlations.

Many correlations have been developed for predicting turbulent mixing for a variety of geometries and flow conditions. The most applicable correlations to Pressurized Water Reactor (PWR) fuel bundles involve a turbulent mixing coefficient and a turbulent mixing

factor. Rowe and Angle [5] developed a correlation using a turbulent mixing coefficient, β, to correlate turbulent crossflow per unit length, w'_{ij}, between channel i and channel j. The equation is as follows:

$$w'_{ij} = \beta_{ij}\bar{G}c \tag{1.5}$$

where $\bar{G}$ is the average axial mass flux of the two subchannels, and c is the rod to rod spacing or rod gap. The following is the correlation for β:

$$\beta_{ij} = K\left[\frac{D_e}{z_{ij}}\right]Re^{\frac{-m}{2}} \tag{1.6}$$

where K and m are empirical constants, Re is the axial Reynolds number, and z_{ij} is the effective mixing distance between the two subchannels, typically taken to be the rod pitch. This correlation is available in the COBRA-EN subchannel analysis code [6]. Castellana [2] determined $\beta = 0.0071\left(\frac{D_e}{c}\right)Re^{-0.10}$, which, for his geometry, gave K as 0.02835. His data showed too much scatter in Re, so he accepted the value of the exponent, -0.10, from previous experiments.

An alternate correlation is in the form of a mixing factor, Y [3, 7]. The turbulent crossflow from this correlation is defined as the following:

$$w'_{ij} = Y\frac{\rho S_{ij}\bar{\varepsilon}}{\delta_{ij}} \tag{1.7}$$

where ρ is the density, δ_{ij} is the mixing distance, typically the centroid distance of the two subchannels or the rod pitch, and $\bar{\varepsilon}$ is a reference eddy viscosity taken to be the eddy viscosity in a pipe. The reference eddy viscosity is correlated as follows:

$$\bar{\varepsilon} = \frac{\nu}{20}Re\sqrt{\frac{\lambda_T}{8}} \tag{1.8}$$

where ν is the kinematic viscosity and λ_T is the friction factor in a smooth pipe. The mixing factor is essentially a correction factor that takes into account the difference of the actual eddy viscosity from the reference eddy viscosity and the estimated temperature gradient in the rod gap. Based on previous results of others, Rehme [3] derived a correlation for Y that fit all existing data:

$$Y = \frac{0.7}{\left(S_{ij}/D\right)} \tag{1.9}$$

where D is the rod diameter. The data scatter for this correlation is large, but Rehme noted that this scatter is due to geometric tolerances, flow measurement techniques, and flow perturbations introduced by measuring devices and spacers from the previous experiments. This correlation incorporates the effect of flow pulsations, so it can be used for any geometry. Jeong [7] defined an improved mixing factor that was dependent on the pitch to diameter ratio rather than the gap to diameter ratio:

$$Y_H = 1.5615\left(\frac{\delta_{ij}}{D_e}\right)^{2.013} \tag{1.10}$$

and is valid for both square and triangular lattices. These correlations represent 50 years of research and experimentation, though they can always be improved, and it is hoped that CFD can be used for these improvements instead of newer experiments.

There have been many comparisons between CFD and rod bundle experiments in the past few years with promising results. Hosokawa [8] performed an experiment on a 2x2 bundle and simulated the same experiment using CFD. He chose the standard k-ε turbulence model and the Launder-Sharma k-ε turbulence model [9]. He found that the CFD results agreed well with the experimental results, with a few caveats. The velocity distribution was predicted to be flatter than was measured, and the flow rate was predicted to be higher than measured in the center subchannel. The k-ε model does not take into account anisotropy in turbulence, so that could be a source of error and an improvement that could be made to increase the applicability of this model for rod bundles. Conner [10] performed a validation of CFD in rod bundles with spacer grids under low Reynolds number conditions, using the renormalization group (RNG) k-ε turbulence model [9]. He found the results matched the experimental data well, but this data is for low Reynolds number, so it also does not reflect actual reactor conditions. Liu [11] performed an experiment using spacers with mixing vanes and compared his results to predictions from CFD. He cited others' work that concluded the standard k-ε model under-predicted turbulence intensities, so he chose the Reynolds stress turbulence model (RSM) [9]. This model solves transport equations derived from the

Navier-Stokes equations, so it is inherently more accurate than the k-ε model, but it is not as robust and does not converge as well [12]. He found that the CFD results matched the experimental data well, except for the decay trend of the Nusselt number, which he said may be improved by using a finer mesh or by better refining the turbulence model. These experiments show that CFD can match experimental data, though more testing and development is necessary.

2 Subchannel Analysis Sensitivity Studies

An analysis was done to measure the sensitivity of temperature and mass flow through a rod bundle to changes in the following: turbulent crossflow, lateral crossflow loss coefficient, and heat transfer coefficient. These terms are all expected to be largely different from the assembly averaged values in regions near and inside of a spacer grid. This preliminary analysis was performed by varying the value of each of the above terms in COBRA-EN, using a typical 17x17 PWR fuel bundle provided in the code package from the Radiation Safety Information Computational Center (RSICC) at Oak Ridge National Lab. The relative pin powers for a quarter of the assembly are shown in Figure 2-1 below. The assembly has a total of 25 water rods (zero power), 9 of which are seen below in the quarter assembly. The bundle was modeled using eighth core symmetry with and without heat.

0.9034	0.9014	0.9001	0.8992	0.8930	0.8840	0.8759	0.8702	0.8386
0.9660	0.9561	0.9559	0.9614	0.9505	0.9334	0.9192	0.9075	0.8702
0.0000	0.9772	0.9787	0.0000	0.9856	0.9682	0.9434	0.9192	0.8759
0.9895	0.9774	0.9792	0.9928	1.0000	0.0000	0.9682	0.9334	0.8840
0.9930	0.9804	0.9819	0.9947	0.9980	1.0000	0.9856	0.9505	0.8930
0.0000	0.9885	0.9895	0.0000	0.9947	0.9928	0.0000	0.9614	0.8992
0.9943	0.9812	0.9811	0.9895	0.9819	0.9792	0.9787	0.9559	0.9001
0.9936	0.9817	0.9812	0.9885	0.9804	0.9774	0.9772	0.9561	0.9014
0.0000	0.9936	0.9943	0.0000	0.9930	0.9895	0.0000	0.9660	0.9034

Figure 2-1. Relative pin powers for a quarter assembly of a typical 17x17 fuel bundle.

2.1 Turbulent Crossflow

Turbulent crossflow represents momentum and energy transfer due to eddy currents in the fluid as described previously, and is denoted as w'_{ij}. This study used the default correlation in COBRA-EN for turbulent crossflow shown below:

$$w'_{ij} = 0.02 s_{ij} \overline{G_{ij}} \tag{2.1}$$

where s_{ij} is the gap spacing and $\overline{G_{ij}}$ is the average axial mass flux around the gap. This turbulent crossflow term was artificially set to zero, halved, doubled, and multiplied by 1.5 to give a range of sensitivity data. The unheated cases showed no dependence of enthalpy or mass flux on turbulent crossflow, as expected, because there were no temperature gradients to drive the energy transfer. Figure 2-2 below shows the axial distribution of enthalpy and mass flux in the hot channel for the heated case. The legend shows the multiplier for the turbulent crossflow term, with "nom" referring to the nominal case. The smaller graphs to the right are zoomed pictures near the exit of the channel to better show the differences in each case.

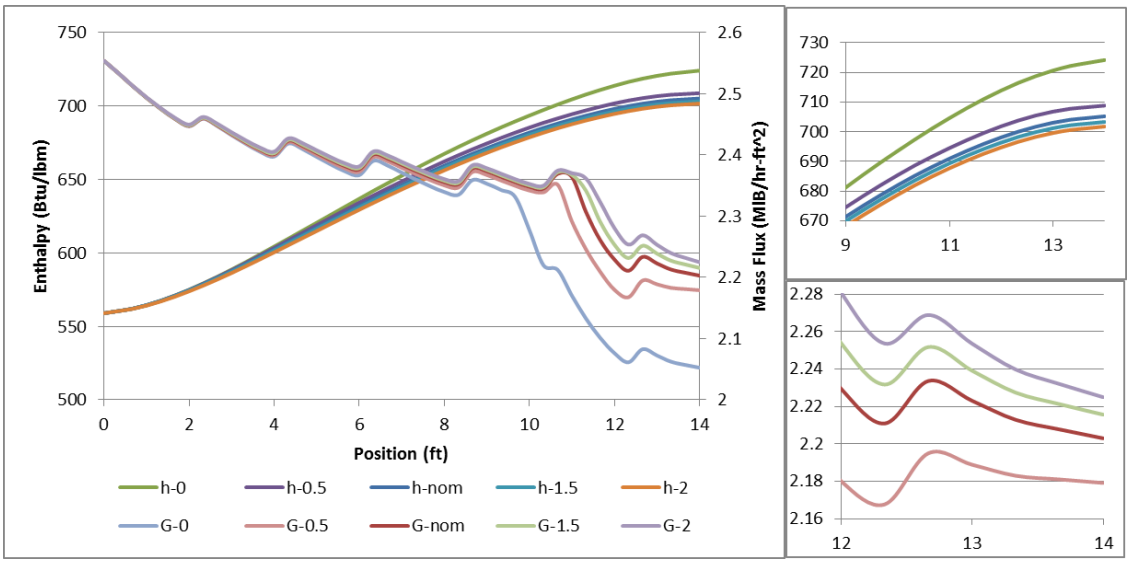

Figure 2-2. Axial distributions for enthalpy and mass flux in the hot channel for turbulent crossflow sensitivity.

The results in Figure 2-2 show that the exit enthalpy in the hot channel will vary by less than 1% if the turbulent crossflow varies by 50%, and increasing turbulent crossflow results in decreasing enthalpy sensitivity. When turbulent crossflow is not allowed, the hot channel becomes hotter, by about 3%, since its energy is no longer transported to the colder channels via turbulent interchange, and vice versa. These results also show that turbulent crossflow is important in moderating enthalpy difference between subchannels, especially without mixing devices. The mass flux results are similar to the enthalpy results. They vary by less than 1% for all the turbulent crossflow values analyzed, except for no turbulent crossflow, which is about 6.8% from nominal.

Subchannel methods treat spacer grids as points at which a loss coefficient is specified. The spacer grid could cause a large perturbation in the turbulent crossflow that would not be captured by the subchannel method. Since the spacer grids are not very long axially compared to the bundle length, this possible inaccuracy may not be very important. However, the length of the spacer grids could be significant compared to the development of

phenomena of interest, especially grids that contain mixing devices, so this effect will be explored.

2.2 Lateral Crossflow Loss Coefficient

The lateral crossflow loss coefficient represents resistance to crossflow between adjacent subchannels. The default value is 0.5 for an average fuel bundle. The sensitivity analysis was performed by setting the loss coefficient to the following values: 0, 0.25, 1, 3, and 10. The larger values were chosen because the smaller values showed no impact in enthalpy and axial mass flux.

Figure 2-3 below shows the axial distribution of enthalpy and flow in the hot channel. The legend shows the value for the lateral crossflow loss coefficient, with "nom" referring to the nominal case of 0.5.

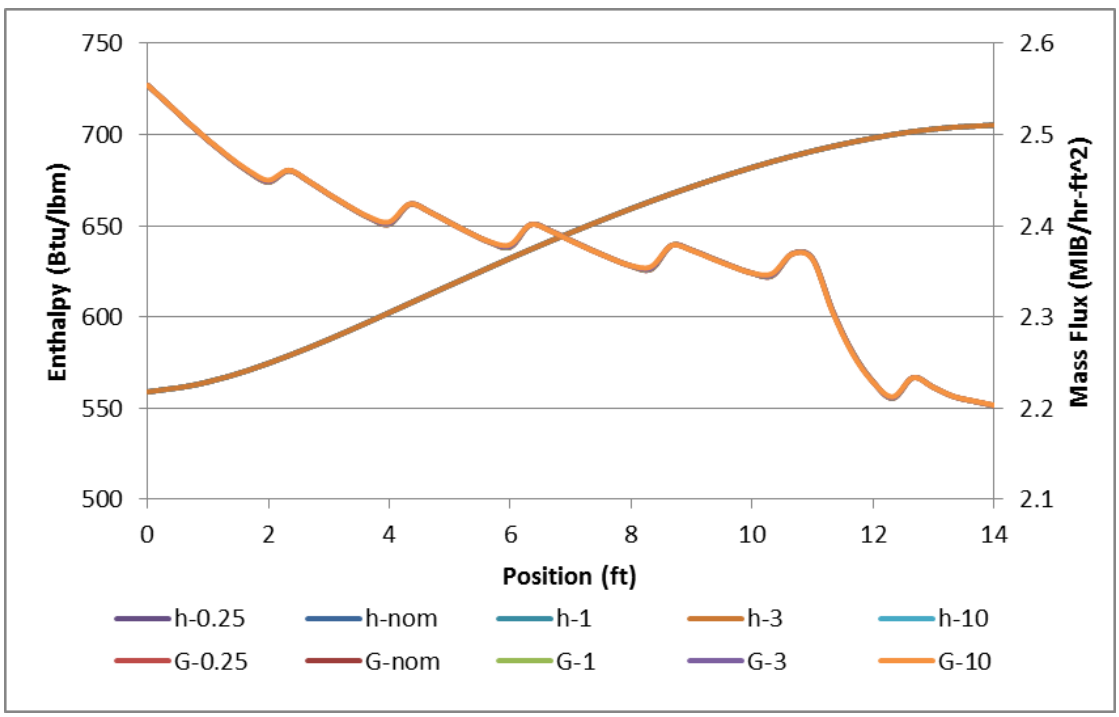

Figure 2-3. Axial distributions for enthalpy and mass flux in the hot channel for crossflow loss coefficient sensitivity.

As seen above, variation in the lateral crossflow loss coefficient had no noticeable effect on the axial enthalpy and flow distributions. This lack of effect is expected since enthalpy and axial mass flux are not highly dependent on the diversion crossflow from subchannel to subchannel.

2.3 Heat Transfer Coefficient

The heat transfer coefficient in and around a spacer grid is not known with much accuracy. COBRA-EN takes into account the effect of a spacer grid on the heat transfer coefficient by slightly increasing it at the spacer grid location, but it is difficult to accurately predict the heat transfer coefficient in the spacer grid region due to a lack of resolution. The heat transfer coefficient could differ greatly in the spacer grid region as compared to the assembly averaged value, so this sensitivity study was performed for values of heat transfer coefficient up to a 30% difference from nominal. The heat transfer coefficient was multiplied by the following values: 0.7, 0.8, 0.9, 1.1, 1.2, and 1.3.

Figure 2-4 shows the axial distribution of the wall temperature of the hot rod for each of the heat transfer coefficient multipliers. The graph is zoomed at the lower portion of the rod to better show the sensitivity effects, since they are small at higher positions due to the onset of nucleate boiling. Table 2-1 shows that the point at which the onset of nucleate boiling occurs is highly dependent on the heat transfer coefficient, and varies by 100% for the range of heat transfer coefficient studied in this analysis. Thus, predicting the heat transfer coefficient accurately will lead to more confidence in predicting the onset of nucleate boiling.

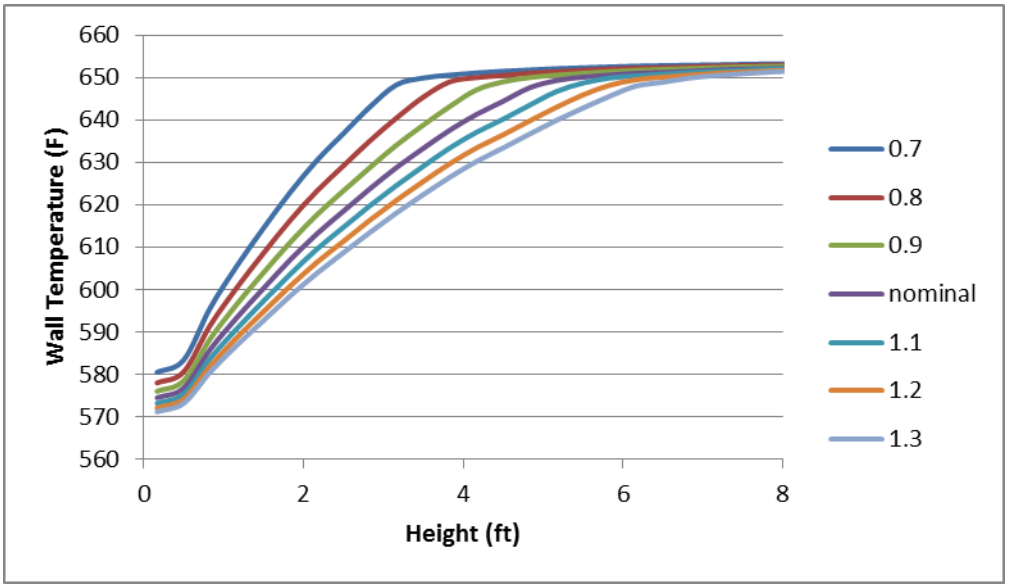

Figure 2-4. Axial distribution of the wall temperature of the hot rod.

Table 2-1. Onset of nucleate boiling for the varying heat transfer coefficients.

Case	Onset Point(ft)	Rod Temperaure
70%	3.5	649.9
90%	4.5	648.6
normal	5.166	649
110%	5.833	649.4
130%	6.833	649.2

The wall temperature can vary by about 5.6% for the range of heat transfer coefficient studied in this analysis. This variation in wall temperature shows that the heat transfer coefficient can have a noticeable effect on the wall temperature. If the heat transfer coefficient is significantly different in a spacer grid region, then subchannel analysis may poorly predict the rod wall temperature in that region. As seen in the CFD results section later, the heat transfer coefficient is significantly larger in the spacer grid region due to a higher axial flow through the region because of the smaller area. This increase in heat transfer coefficient leads to a drop in the wall temperature, so the predictions of COBRA-EN are conservative for thermal margins.

3 Turbulent Mixing Experiments

3.1 Introduction of Experiments

Three turbulent mixing experiments were duplicated with the use of CFD, utilizing the CFX package within ANSYS [13]. They are as follows: a 4x4 bundle [14], a 5x5 bundle [2], and a 2x2 bundle [8]. The 4x4 and 5x5 bundles consisted of rods and a channel box made of stainless steel. The rods were heated by an electrical current passing through the center of each rod to produce a constant heat flux at the wall. This heat source was modeled in CFX as a constant heat flux placed at the boundary between the rods and the water, equivalent to the heat flux the electrical current would provide at that location. The 2x2 bundle was not heated, and it used rods and a channel box made of a transparent material in order to use a camera to determine flow patterns.

3.2 Pressure Drop Calculations

Unheated versions of the 4x4 bundle and the 5x5 bundle were modeled and run in CFX and COBRA-EN, in order to ensure the geometric models were set up correctly and the pressure drop was comparable for both tools. Two cases with different mass flow rates were chosen for each of the bundles. The results are shown in Table 3-1. The pressure drop is calculated directly by COBRA-EN, while the pressure drop was calculated from the CFX results by taking the difference of the average absolute pressure at the inlet and the average absolute pressure at the outlet.

Table 3-1. Unheated pressure drop for the 4x4 and 5x5 bundles from CFX and COBRA.

Case	Inlet Enthalpy (BTU/lbm)	Average Mass Flux (lbm/hr-ft^2)	Pressure (psia)	COBRA	CFX	%difference
4x4 Case 22	172	1.01E+06	1200	2.5	2.49	0.40%
4x4 Case 50	225	2.99E+06	1200	4.78	4.78	0.00%
5x5 Case 1	325	1.55E+06	1500	3.90	4.01	2.78%
5x5 Case 2	325	2.75E+06	1500	6.95	7.22	3.81%
5x5 Case 1 no spacer	325	1.55E+06	1500	3.3	3.28	0.61%
5x5 Case 2 no spacer	325	2.75E+06	1500	5.07	5.05	0.40%

Table 3-1 shows for the 4x4 bundle, the pressure drop is almost identically calculated by both COBRA-EN and CFX. The difference in pressure drop for the 5x5 bundle is slightly larger, but it is still close. The 4x4 bundle does not have spacer grids, while the 5x5 bundle does, so the spacer grid could be the cause of the lower accuracy. For this reason, the 5x5 bundle was also run with no spacer grids. This run shows that the spacer grid is the cause of the disagreement, since the difference in pressure drop is less without the spacer grid. This phenomenon would be expected since COBRA does not resolve the spacer grid, but rather uses a loss coefficient provided by a correlation. This loss coefficient could be iterated upon to make the pressure drop match the CFX results, but this iteration was not performed because it would not noticeably alter the results for the other parameters. Overall, these results show that the pressure drop is consistently predicted with the two simulation tools. Since pressure drop and wall heat transfer both depend heavily on the fluid distribution in the vicinity of the wall, these results also provide confidence in the prediction of wall heat transfer coefficient and wall temperature.

3.3 4x4 Bundle Experiment

The 4x4 bundle utilized 5 cylindrical spacers designed to minimize flow disturbance, and as such were not modeled in CFX, since they would not alter the results in any meaningful manner. The geometry for this bundle is shown in Table 3-2. The average exit

enthalpy and mass flux of two of the inner subchannels and of the entire bundle were measured. The measured subchannels were numbered 5 and 11 as shown in Figure 3-1. Most of the cases reported had some degree of boiling, so only cases that were single-phase throughout were chosen for simulation in CFX.

Table 3-2. Geometry in inches for the 4x4 bundle.

Diameter	Pitch	Rod to Wall	Rod to Rod	Height
0.422	0.555	0.148	0.133	60

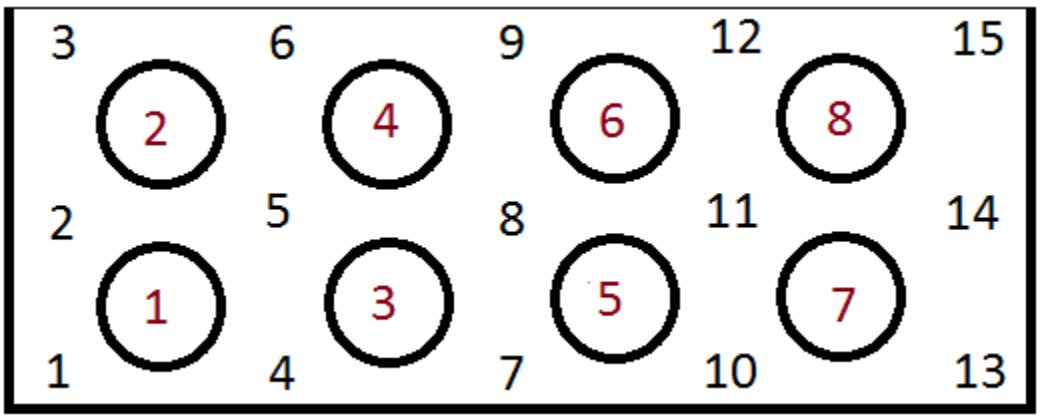

Figure 3-1. Diagram of the 4x4 bundle.

Five different cases were simulated with both COBRA-EN and CFX. The conditions for these cases are shown in Table 3-3 below, numbered as they were in the reference paper [14]. The power was converted to an average heat flux from which the hot and cold heat fluxes were obtained. The hot heat flux was 108% of the average and the cold heat flux was 92% of the average. Rods 1-4 were the hot rods and rods 5-8 were the cold rods. The chosen cases provide a range of inlet temperatures, along with two distinct flow rates.

Table 3-3. Parameters for each case of 4x4 bundle.

Case	Pressure (psia)	Inlet Enthalpy (BTU/lbm)	Power (MW)	Avg Mass Flux (lbm/hr-ft^2)
22	1200	172	0.99	1.01E+06
23	1200	225	0.98	1.02E+06
24	1200	277	1.00	1.01E+06
50	1200	225	1.50	2.99E+06
51	1200	267	1.45	2.98E+06

Two different mesh sizes were utilized for this bundle. The first mesh was the coarse mesh seen in Figure 3-2. It predicted the exit enthalpies in the higher flow cases significantly worse than for the lower flow cases, and had a higher error for the average exit enthalpy. For this reason a finer mesh was created, seen in Figure 3-3, and a comparison of the two meshes was performed. The coarse mesh has 2.1 million elements with an average aspect ratio of about 2.75, while the fine mesh has 17.3 million elements with an average aspect ratio of about 12.5.

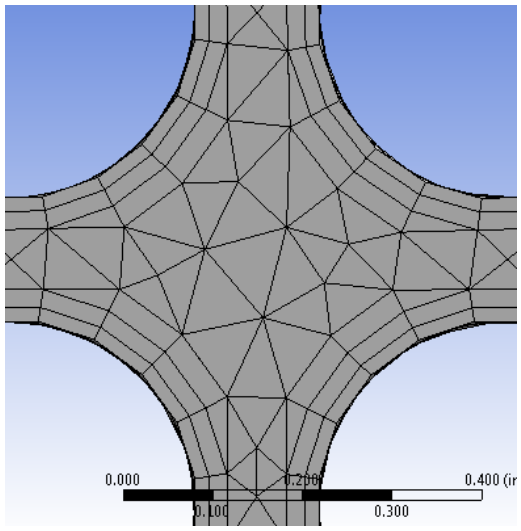

Figure 3-2. Diagram of the coarse mesh for 4x4 bundle.

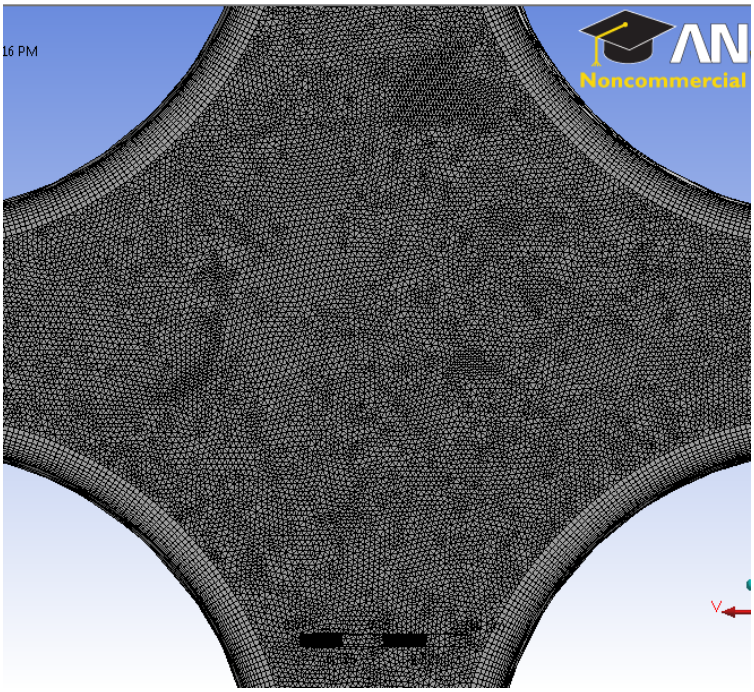

Figure 3-3. Diagram of the fine mesh for 4x4 bundle.

Table 3-4 and Table 3-5 show the average exit enthalpy for the two measured channels and for the whole bundle. The locations of each channel are shown in the bundle diagram in Figure 3-1. "CFX" refers to the CFX results and "EXP" refers to the experimental results. The percent errors are negative for under-predicting the enthalpy as compared to the experiment and vice versa. These results show that the fine mesh predicts the average exit enthalpy significantly better than does the coarse mesh. This metric means that the fine mesh does a better job of accounting for the correct heat input into the rod bundle. The coarse mesh over-predicts average exit enthalpy by 4-6%, so the total heat input would be expected to be over-predicted by about that amount. The fine mesh was not as accurate in the prediction of individual channel exit enthalpies as it was for prediction of the bundle average enthalpy. The enthalpy is under predicted for both subchannels in the lower flow cases. In the high flow cases, channel 11 was measured to be hotter than channel 5, even though channel 5 would be expected to be hotter since it is surrounded by higher powered rods. This anomaly occurs in other cases as well, and the authors of the study

provide no explanation for this behavior. The CFX results show channel 5 to be hotter than channel 11 as would be expected. Based on the results, the fine mesh is considered to be better than the coarse mesh because it captures the heat input with greater accuracy, even though the distribution of that heat may not be as correct.

Table 3-4. Exit enthalpy results for the coarse mesh of the 4x4 bundle.

Case	CFX h5	EXP h5	%error	CFX h11	EXP h11	%error	CFX havg	EXP havg	%error
22	362.896	355	2.22%	335.612	342	-1.87%	333.085	313	6.42%
23	412.141	401	2.78%	385.972	388	-0.52%	383.357	362	5.90%
24	470.671	459	2.54%	443.482	444	-0.12%	440.675	420	4.92%
50	323.594	302	7.15%	309.551	310	-0.14%	308.035	297	3.72%
51	370.860	345	7.50%	355.310	354	0.37%	351.440	337	4.28%

Table 3-5. Exit enthalpy results for the fine mesh of the 4x4 bundle.

Case	CFX h5	EXP h5	%error	CFX h11	EXP h11	%error	CFX havg	EXP havg	%error
22	342.877	355	-3.41%	320.857	342	-6.18%	314.158	313	0.37%
23	393.625	401	-1.84%	371.693	388	-4.20%	365.062	362	0.85%
24	451.278	459	-1.68%	428.526	444	-3.49%	421.673	420	0.40%
50	314.525	302	4.15%	302.432	310	-2.44%	298.938	297	0.65%
51	356.535	345	3.34%	344.406	354	-2.71%	340.918	337	1.16%

The above percent errors are absolute error, based on the value of the exit enthalpy. A A relative percent error, based on the difference of the inlet enthalpy from the exit enthalpy, may provide a better sense of the actual error in the calculation. The relative errors are shown in

Table 3-6 below. Since these are relative errors, they would be expected to be greater than the absolute percent error seen above.

Table 3-6. Relative errors in enthalpy for both meshes in the 4x4 bundle

	Fine Mesh			Coarse Mesh		
Case	h5	h11	havg	h5	h11	havg
22	-6.62%	-12.44%	0.82%	4.31%	-3.76%	14.24%
23	-4.19%	-10.00%	2.24%	6.33%	-1.24%	15.59%
24	-4.24%	-9.27%	1.17%	6.41%	-0.31%	14.46%
50	16.27%	-8.90%	2.69%	28.04%	-0.53%	15.33%
51	14.79%	-11.03%	5.60%	33.15%	1.51%	20.63%

Two different turbulent mixing correlations were used in COBRA-EN: the default correlation, which sets a constant β equal to 0.02, and a varying β with K equal to 0.0296 and m equal to -0.2. The K and m values were taken from the correlation developed by Castellana [2]. The varying β correlation will produce less turbulent mixing than would the default, so it would be expected that the hot channels would become hotter, and the cold channels would become colder, when the two correlations are compared. Table 3-7 shows these results and the percent error for the varying β correlation with respect to the experimental values, where "def" refers to the default correlation and "beta" refers to the varying β correlation. Both correlations produce the same average exit enthalpy, so that value is shown alone. As with the fine mesh in CFX, COBRA-EN predicts the average exit enthalpy with very good accuracy, but not as well for the individual channels. It is interesting that the CFX and COBRA-EN results match each other very closely, suggesting both models can be used to predict enthalpy distributions with the same level of accuracy.

Table 3-7. Exit enthalpy results from COBRA-EN for the 4x4 bundle.

Run	def h5	beta h5	%error	def h11	beta h11	%error	havg	%error
22	331.2088	338.7853	-4.57%	316.0084	318.9497	-6.74%	317.986	1.22%
23	381.1739	388.8609	-3.03%	366.1941	369.2232	-4.84%	368.095	0.83%
24	438.0122	446.1251	-2.80%	422.5399	425.7643	-4.11%	424.461	0.66%
50	306.9167	311.6914	3.21%	298.7883	300.8106	-2.96%	299.717	0.26%
51	346.4852	351.2121	1.80%	338.5847	340.6031	-3.78%	339.469	-0.43%

The results for the 4x4 bundle demonstrate that CFX predicts exit enthalpy in rod bundles reasonably well. It predicts the average exit enthalpy almost perfectly, but is less accurate for individual channels. It under-predicts the hot channel for some cases, which would be troublesome for predicting thermal limits that need the hot channel predicted with conservatism. Since the error for the individual channels is large in some cases, it can be concluded that CFX may not predict mixing among these channels with a large degree of accuracy.

3.4 5x5 Bundle Experiment

The 5x5 bundle experiment was designed to find an average turbulent mixing coefficient, β, for the bundle. It utilized 4 egg crate spacer grids to hold the rods in place. The small dimples in the spacer grid that touch the rod were not modeled in CFX, since they would not significantly alter flow. The dimensions of the spacer grid used were not given, so the dimensions in this analysis were based on an available physical replica of a spacer grid, modified to achieve a desired loss coefficient. The geometry for this bundle is shown in Table 3-8. The left two columns of rods in Figure 3-4 were powered at ten times the amount of the right three columns of rods in order to make mixing more profound. All exit temperatures were measured by a 0.07 inch diameter platinum resistance thermometer placed in the center of the channel. These temperatures were converted into enthalpy, and then a constant value of β was determined for the bundle at varying power and flow conditions. The exit enthalpy was recorded from CFX by taking an average over the area the thermometer would occupy.

Table 3-8. Geometry in inches for the 5x5 bundle.

Diameter	Pitch	Rod to Wall	Rod to Rod	Spacer width	Spacer wall thickness	Height
0.422	0.563	0.115	0.141	2.845	0.03	72

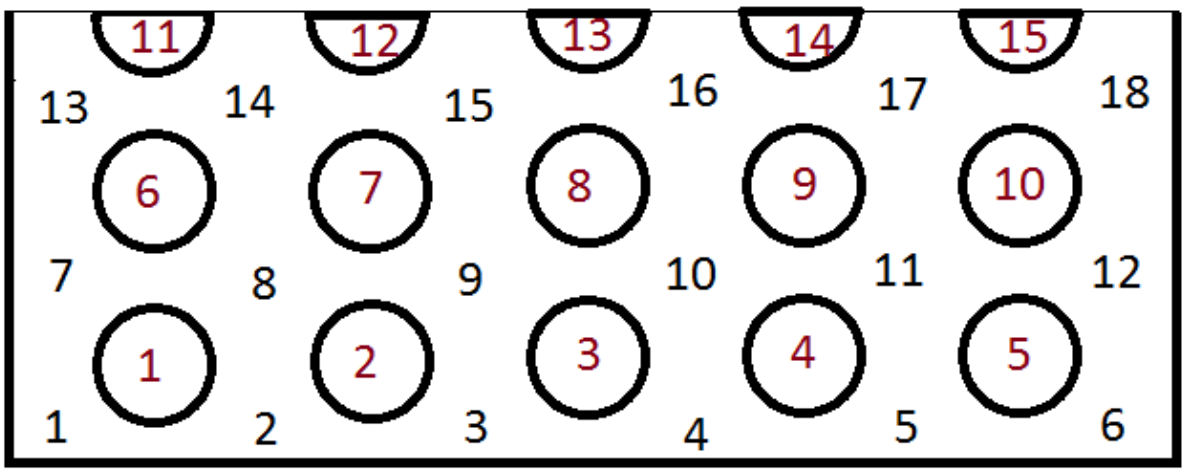

Figure 3-4. Diagram of the 5x5 bundle.

Two fine mesh cases were run for the 5x5 bundle. The mesh was similar to that shown in Figure 3-3, with 68.58 million elements and an average aspect ratio of 7. Table 3-9 shows the input parameters for each case. An inlet enthalpy was not specified, so it was chosen to be 325 BTU/lbm, which is close to the lower end of the experimental data range. The inlet enthalpy should not have an effect on mixing as long as the entire bundle is single phase. The given conditions were pressure, average mass flux and hot heat flux. The cold heat flux was then calculated by dividing the hot heat flux by a factor of 10.

Table 3-9. Parameters for each case for the 5x5 bundle.

Case	Pressure	Inlet Enthalpy (BTU/lbm)	Avg Mass Flux (lbm/hr-ft^2)	Hot Heat Flux (BTU/ft^2-hr)
1	1500	325	1.55E+06	1.9600E+05
2	1500	325	2.75E+06	3.0900E+05

In order to determine β, Castellana [2] defined the relative fit parameter S:

$$S = \sum_{i} \sum_{j} \left[\left(h_{e(i)} - h_{e(j)} \right) - \left(h_{p(i)} - h_{p(j)} \right) \right]^2 \tag{3.1}$$

where h is the exit enthalpy, i and j refer to adjacent subchannels, e refers to experimental data, and p refers to predicted data from COBRA-EN. This summation was performed for adjacent inner subchannels (numbered 8-11 and 14-17). The predicted enthalpies were found by choosing different constant bundle mixing coefficients as an input to COBRA-EN. This fit parameter was then found for each β and the minimum S corresponded to the appropriate β value for the bundle. This same process was reproduced using CFX as the experimental data. Castellana used COBRA-II [15], while COBRA-EN was used for this analysis. The same turbulent mixing model from COBRA-II was utilized in COBRA-EN, but other differences between the codes could potentially skew the results. The axial nodalization was not given, so a difference in height between each node of a third of a foot was used. A comparison to a finer nodalization yielded an indiscernible change in the resulting β. Table 3-10 shows the results for β for both the experiment and CFX, and Figure 3-5 and Figure 3-6 show the S vs. β graphs for cases 1 and 2 respectively.

Table 3-10. Experimental vs. CFX results for β.

Case	CFX	Experiment
1	0.004	0.0091
2	0.03	0.0078

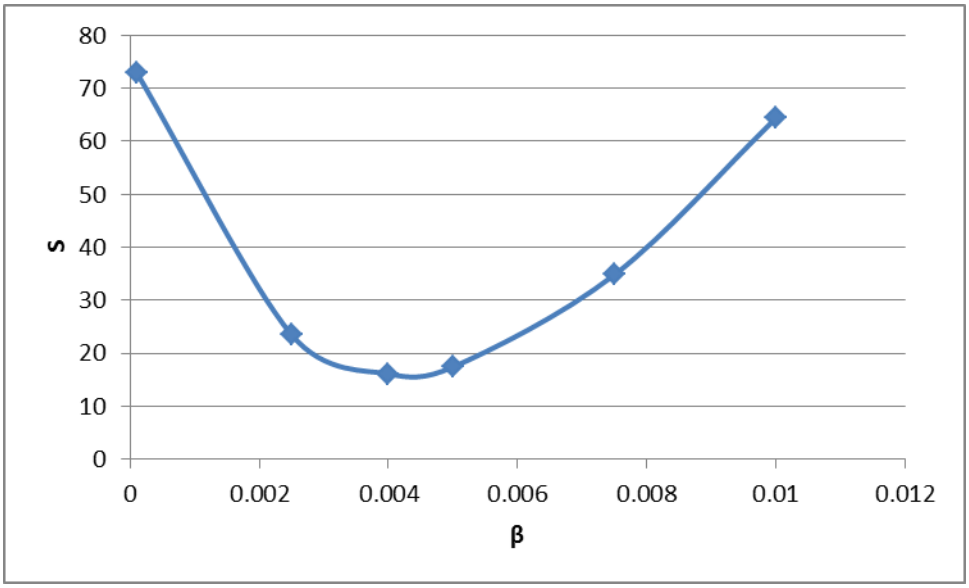

Figure 3-5. S vs β graph for case 1 of the 5x5 bundle.

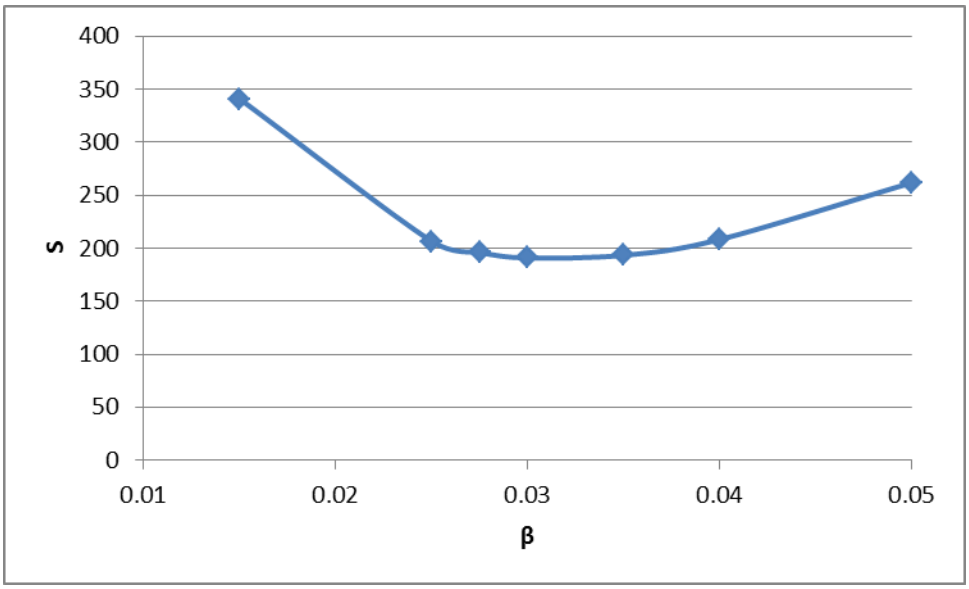

Figure 3-6. S vs β graph for case 2 of the 5x5 bundle.

Table 3-10 shows that for case 1, CFX predicts β to be about half of the value from the experiment, and for case 2, CFX predicts β to be about 4 times the value from the

experiment. These results would imply that CFX predicts mixing poorly for this bundle, but there are other potential sources of error, such as the use of a different version of COBRA, that may account for some of these differences. Figure 3-7 shows the axial distribution of enthalpy predicted in COBRA-EN for each value of β. The variation in the predicted exit enthalpy for case 2 is 3%, while the variation in β is a factor of 4. This difference demonstrates that β is strongly dependent on exit enthalpy, and exit enthalpy is weakly dependent on β. Because of this strong dependence of β on exit enthalpy, this method of mixing comparison may be a poor choice. More recent experiments, such as the 2x2 bundle below, have more direct measurements of turbulence and flow characteristics that would provide a better comparison to determine the accuracy of CFX.

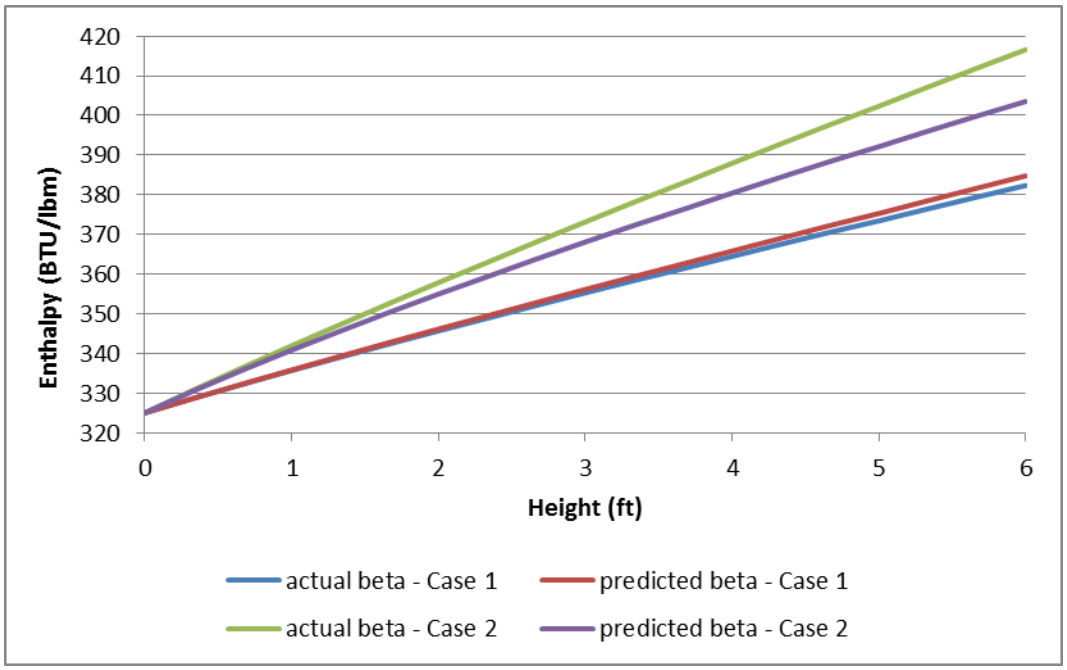

Figure 3-7. Axial enthalpy distribution for different values of β for the hot channel of the 5x5 bundle.

Additional analysis was performed on this bundle to determine the accuracy at which COBRA-EN predicts the axial distribution of enthalpy, wall temperature, and heat transfer

coefficient, especially in the vicinity of the spacer grid. It was assumed that CFX would more accurately describe the trend of these parameters in the vicinity of the spacer grid than COBRA-EN because of the method of solution and the finer scale of CFD. As described previously, subchannel methods do not resolve spacer grids, so these methods would not be expected to accurately predict the flow characteristics within them. The results from CFX provide insight into the effects of spacer grids on the above parameters, and the degree of inaccuracy in the subchannel methods. The results shown are for case 1.

Figure 3-8 shows the axial enthalpy distribution for channel 8. The prediction from COBRA-EN is a linear increase with no effect of the spacer grid, while the CFX data show a drop in enthalpy within the spacer. The decrease in the hot channel fluid enthalpy in the spacer grid region could be explained by an increase in subchannel mixing, leading to higher enthalpies in other colder channels. However, the average fluid enthalpy of the bundle decreased in the spacer grid region (see Figure 3-9), which suggests the fluid lost energy in this region. It is unknown why this loss of energy occurs, but it is not due to conversion to kinetic energy as the fluid increases in velocity, which accounts for a change of only 0.0005 BTU/lbm.

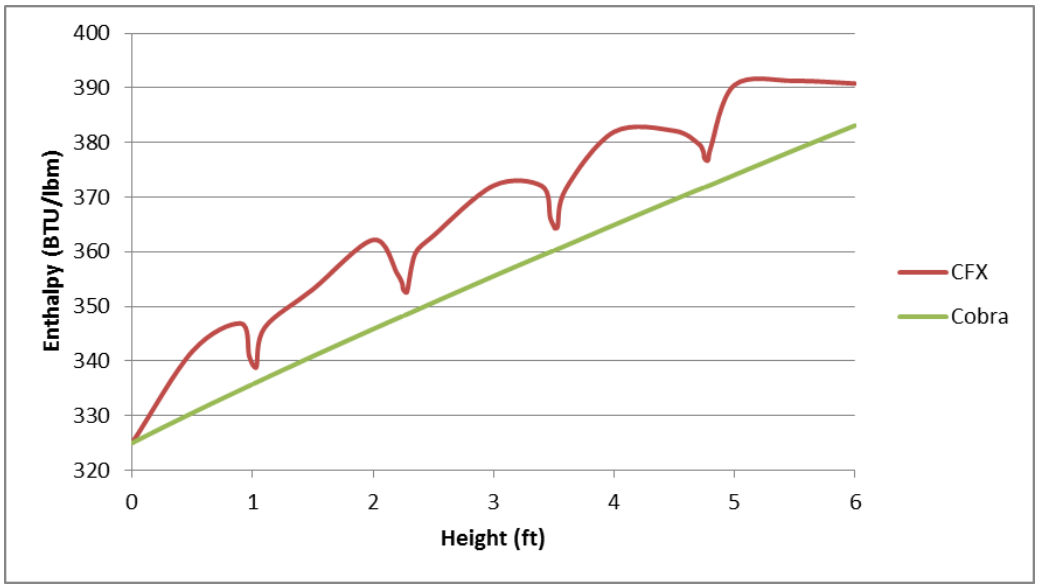

Figure 3-8. Axial enthalpy distribution of channel 8 for the 5x5 bundle.

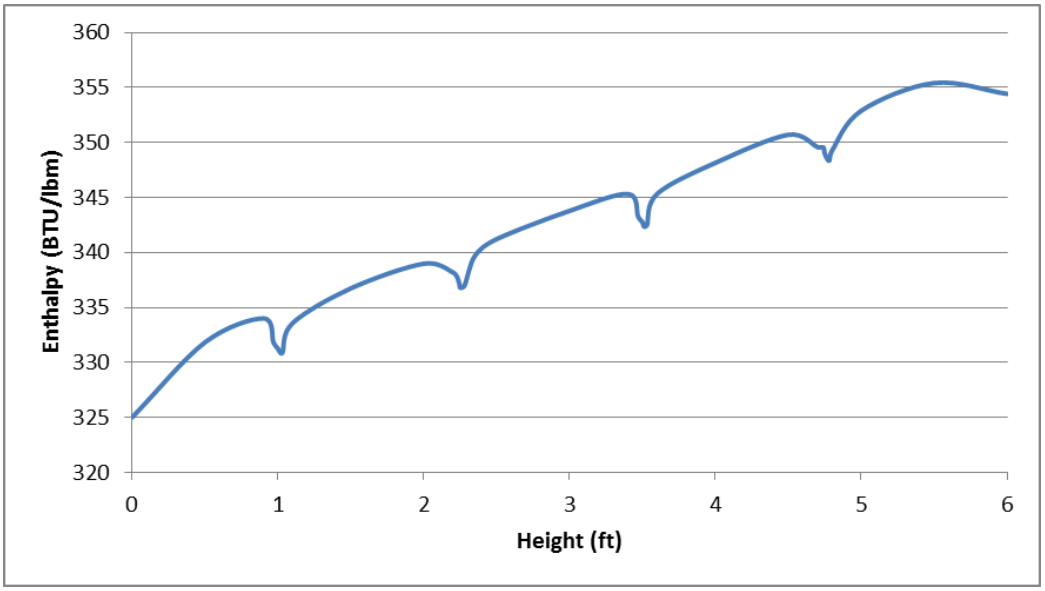

Figure 3-9. Axial distribution of the average fluid enthalpy for the 5x5 bundle.

Figure 3-10 shows the axial wall temperature distribution for rod 1, and Figure 3-11 shows the axial wall heat transfer coefficient distribution for the same rod. The COBRA-EN results show a small effect of the spacer grid on these parameters, but not as large an effect as in the CFX results. The CFX results show a drop in wall temperature and an increase in heat transfer coefficient in the spacer region, which is expected since the axial flow rate is increased due to a reduction in flow area in the region. A close-up view of this effect is shown in Figure 3-12 and Figure 3-13, where the blue line denotes the location of the spacer grid.

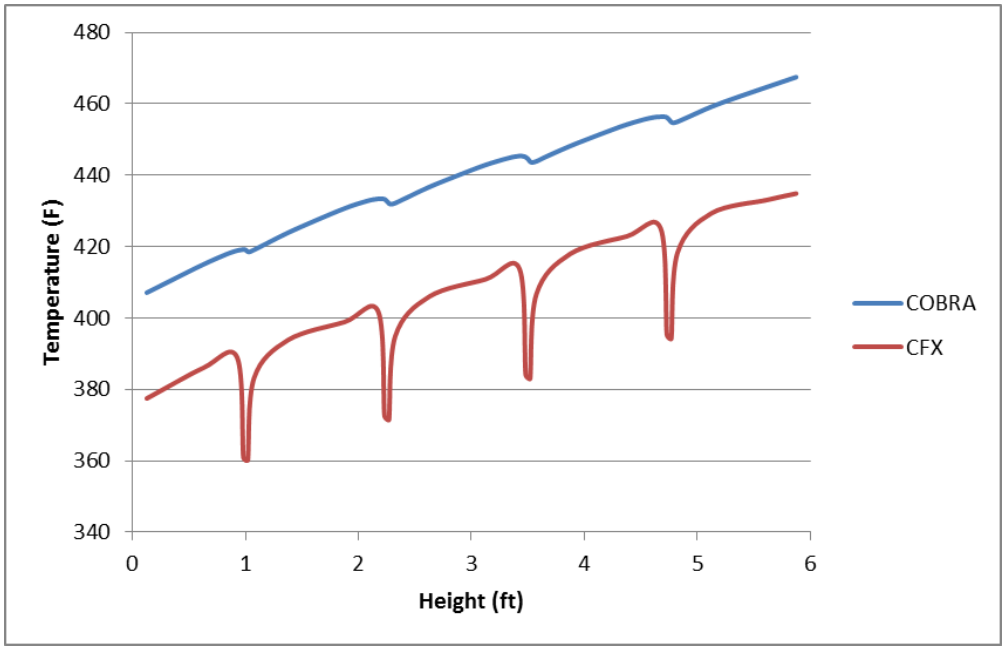

Figure 3-10. Axial wall temperature distribution of the hot rod (rod 1) for the 5x5 bundle.

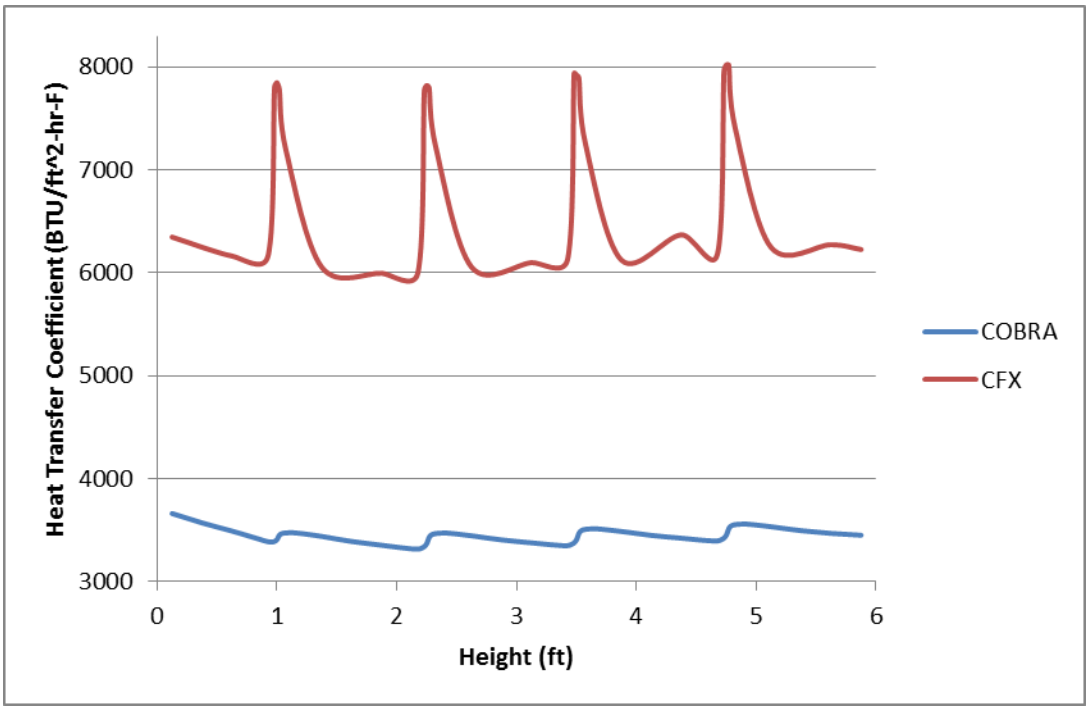

Figure 3-11. Axial heat transfer coefficient distribution of the hot rod for the 5x5 bundle.

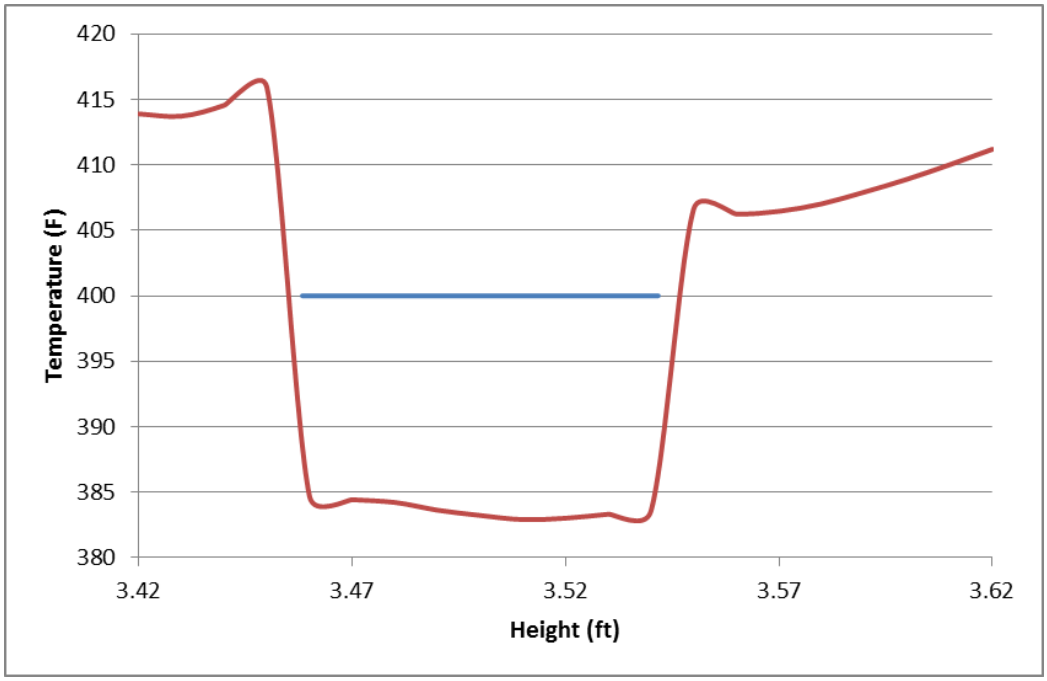

Figure 3-12. Axial wall temperature distribution of the hot rod near the spacer grid.

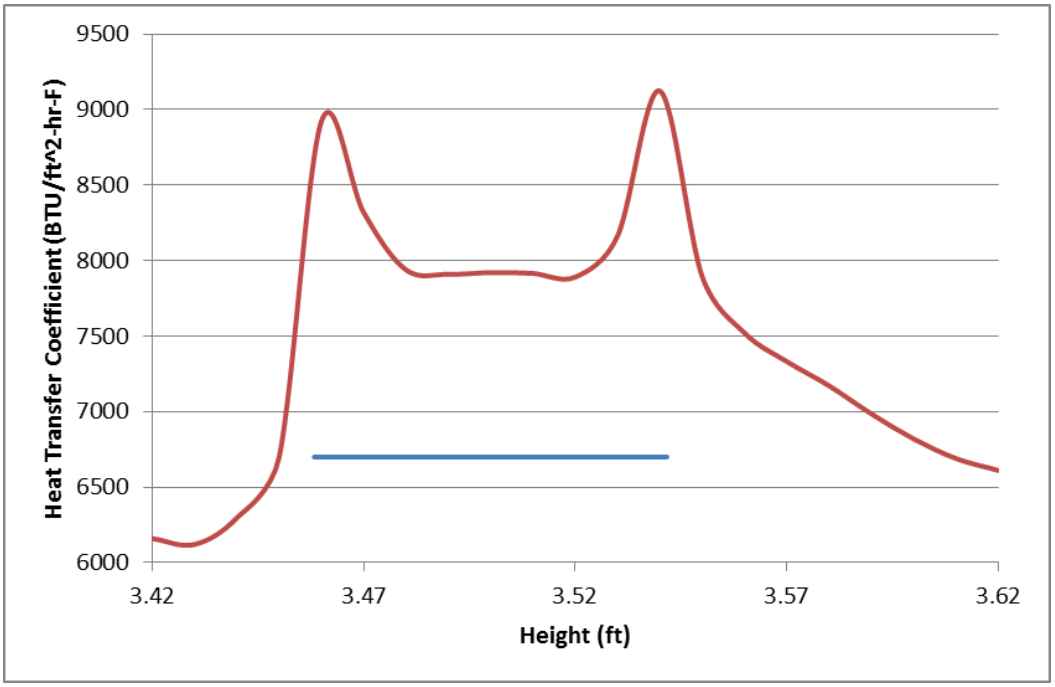

Figure 3-13. Axial wall heat transfer coefficient of the hot rod near the spacer grid

While the CFX results give insight into the behavior of these parameters in the spacer grid region, the values are significantly different than those predicted in COBRA-EN. This discrepancy could be due to the data extraction method employed for the CFX results, though it is unlikely to cause such a large effect. The wall temperature and heat transfer coefficient were not recorded from the solid wall, but rather they were recorded from the fluid location nearest the wall. The likely cause is an inaccurate prediction of the heat transfer coefficient by the k-epsilon turbulence model, as shown in the 17x17 results. This over predicted heat transfer coefficient would lead to a much lower wall temperature prediction.

Figure 3-14 shows the diversion crossflow per unit length from channel 8 to channel 9 as calculated from CFX and COBRA-EN near a spacer grid. COBRA-EN does not resolve the spacer grid, which is why the figure shows a large reversal of flow at the center of the spacer grid. The flow reversal reaches -140 lb/hr-ft. The CFX results illustrate that the crossflow falls and eventually flow reverses at the inlet of the spacer grid, and then the crossflow increases back to its free stream value as the end of the spacer grid nears. The overall trend is a decreasing crossflow with increasing height, though the CFX results fluctuate while the COBRA results are linear.

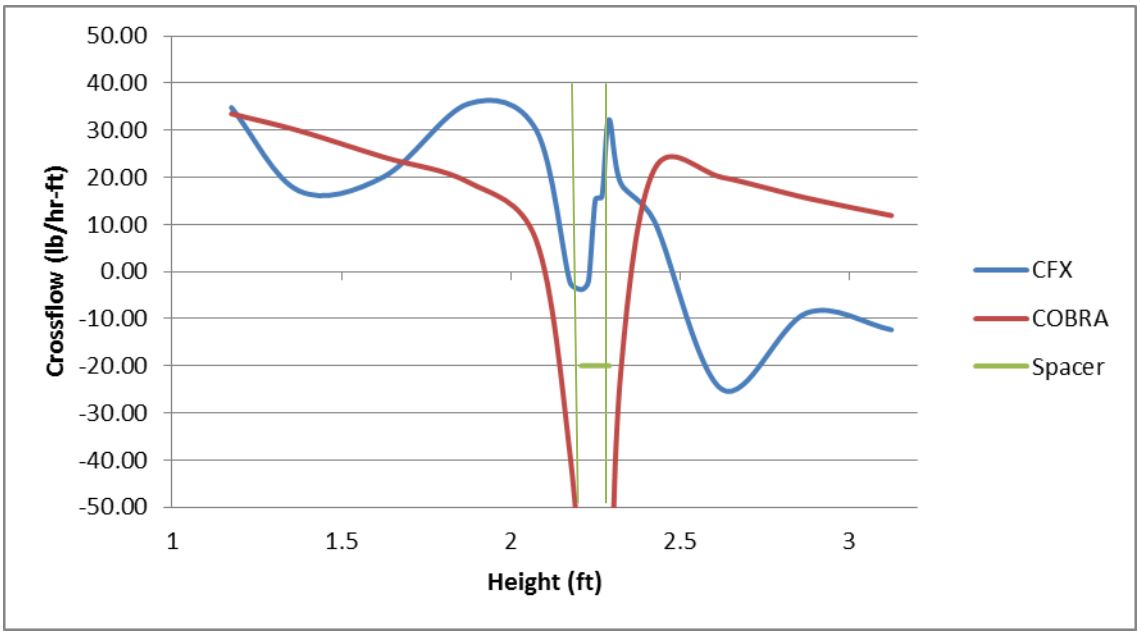

Figure 3-14. Crossflow from channel 8 to channel 9 near a spacer grid.

The 5x5 bundle results demonstrate that CFX predicts the mixing coefficients poorly for this experiment. The mixing coefficients calculated were incorrect by factors of two to four. However, these mixing coefficients have a small effect on enthalpy as shown in Figure 3-7. This small effect means that the thermal margins predicted by CFX will not be impacted significantly. The inaccuracies could be due to the choice of the k-ε turbulence model; other turbulence models may predict the mixing coefficient better. The Reynolds Stress turbulence model was tried, but it was unable to obtain a converged solution for this bundle. Other turbulence models could be tested on this bundle to test if they provide better predictions.

3.5 2x2 Bundle Experiment

The 2x2 bundle was built with stainless steel rods and an acrylic resin channel box [8]. Two of the rods were made of fluorinated ethylene-propylene resin (FEP) pipes to enable measurements of water velocity using particle image velocimetry (PIV) [16]. The FEP pipes contained stainless steel rods, except for in the measurement region, to ensure

structural rigidity. Axial velocity, turbulence intensity, and turbulence kinetic energy were measured, and a CFD comparison using Open FOAM was performed by the experimenters. These parameters were used as the comparison to the CFX results. The full bundle was modeled in CFX with a fine mesh using the k-epsilon, RSM, and k-omega [9] turbulence models. The mesh contained 6.4 million elements with an average aspect ratio of 428. Table 3-11 below shows the input parameters and geometry for the 2x2 bundle in both metric and US customary units. The actual height of the test bundle was 1 m, but it was decided to model it with a 2.5 m height in CFX to allow flow to fully develop. The experimenters used a 5 m height in their CFD calculations. This extra height should not affect the results, as there is no heat, and flow characteristics should not change axially once the flow has become fully developed.

Table 3-11. Parameters for the 2x2 bundle.

Pressure	Inlet Temperature	Inlet Velocity	Height	Diameter	Rod Pitch	Rod to Wall Dist	Rod to Rod Dist
atm	K	m/s	mm	mm	mm	mm	mm
1	298	2	1000	20	25	2.5	5
psia	F	ft/s	ft	in	in	in	in
14.696	76.700	6.562	3.281	0.787	0.984	0.098	0.197

Figure 3-15 and Figure 3-16 show the axial velocity contour from the experiment and the CFX results, respectively, using the same scale. When compared to the experimental results, the predicted axial velocity is lower in the center of the bundle with a flatter overall shape, but the CFX results predict it well overall in both value and shape.

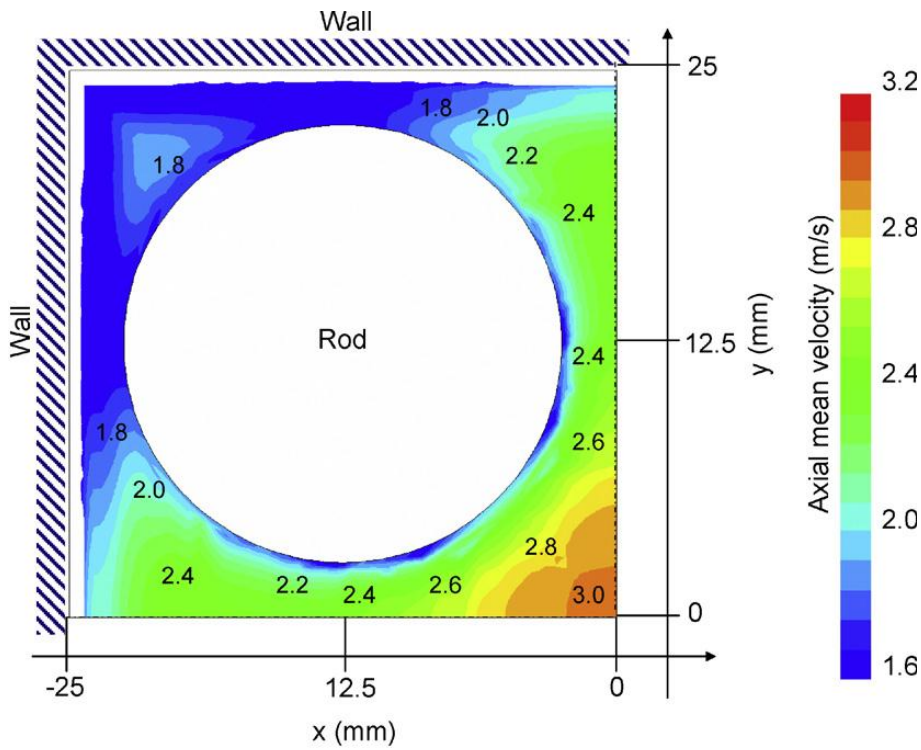

Figure 3-15. Contour graph of the experimental axial velocity for the 2x2 bundle [8].

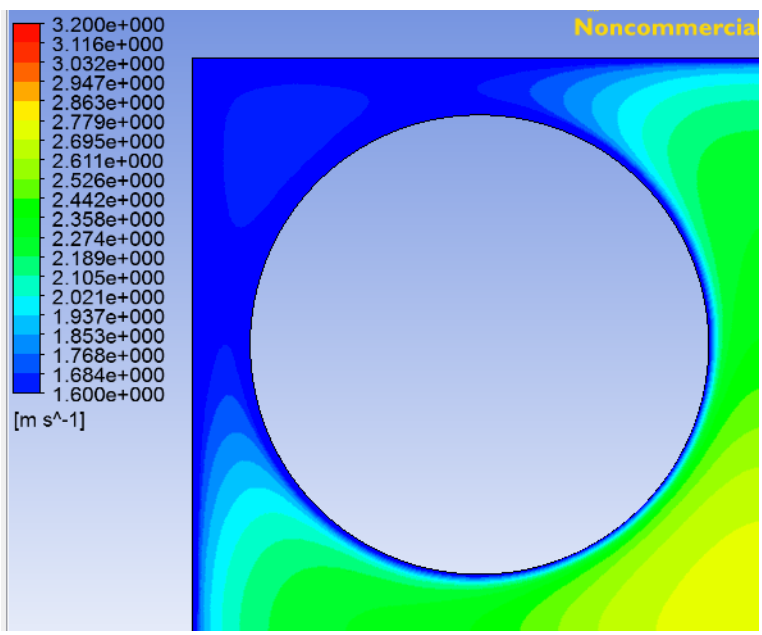

Figure 3-16. Contour graph of the axial velocity using CFX for the 2x2 bundle.

Figure 3-17 and Figure 3-18 show the turbulence kinetic energy distribution for the experiment and CFX, respectively, using the same scale. These figures show that CFX significantly under predicts the turbulence kinetic energy, as the CFX contour shows the turbulence kinetic energy is at the smallest contour for most of the bundle. Figure 3-19 shows the same graph from CFX, but using an order of magnitude smaller scale to show the actual distribution. This figure shows similar trends as compared to the experiment, with turbulence kinetic energy being lower in the center of the channels and higher near the walls. The CFX results show a smoother, more patterned distribution as compared to the jagged and more randomized distribution of the experimental data.

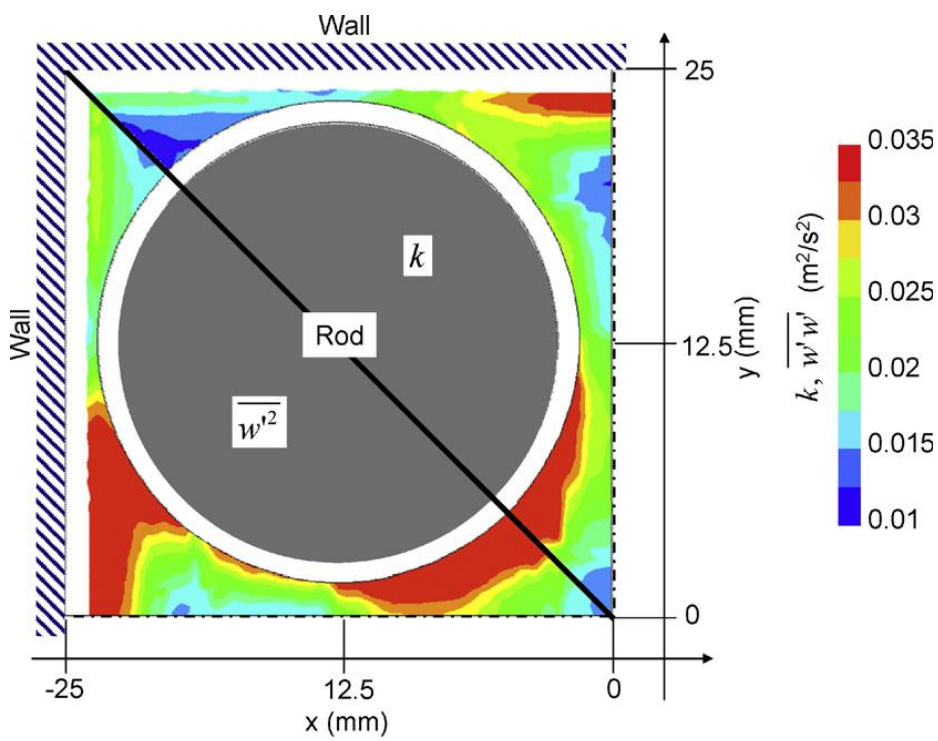

Figure 3-17. Contour graph of the experimental turbulence kinetic energy and turbulence intensity for the 2x2 bundle [8].

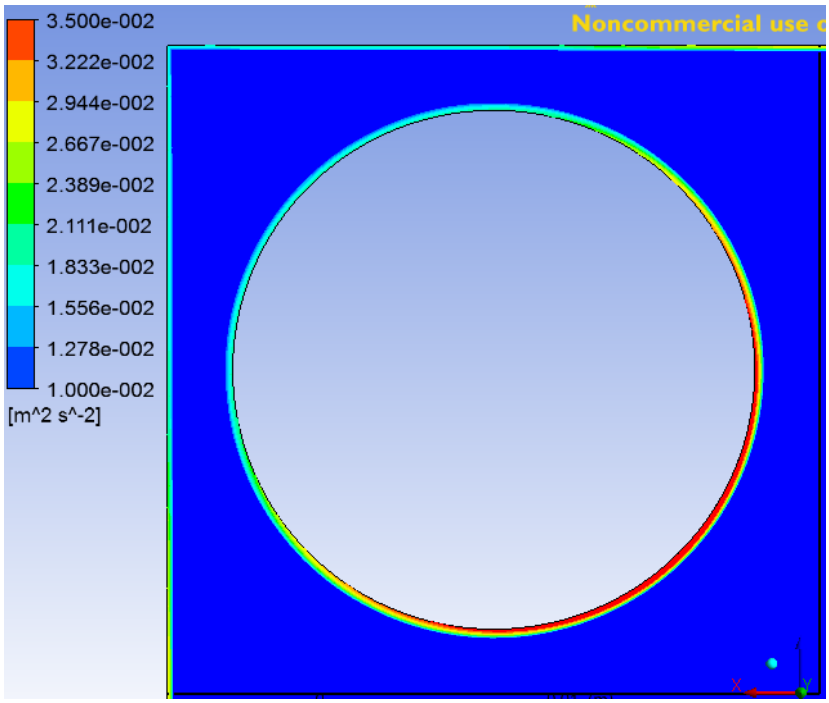

Figure 3-18. Contour graph of the turbulence kinetic energy using CFX for the 2x2 bundle.

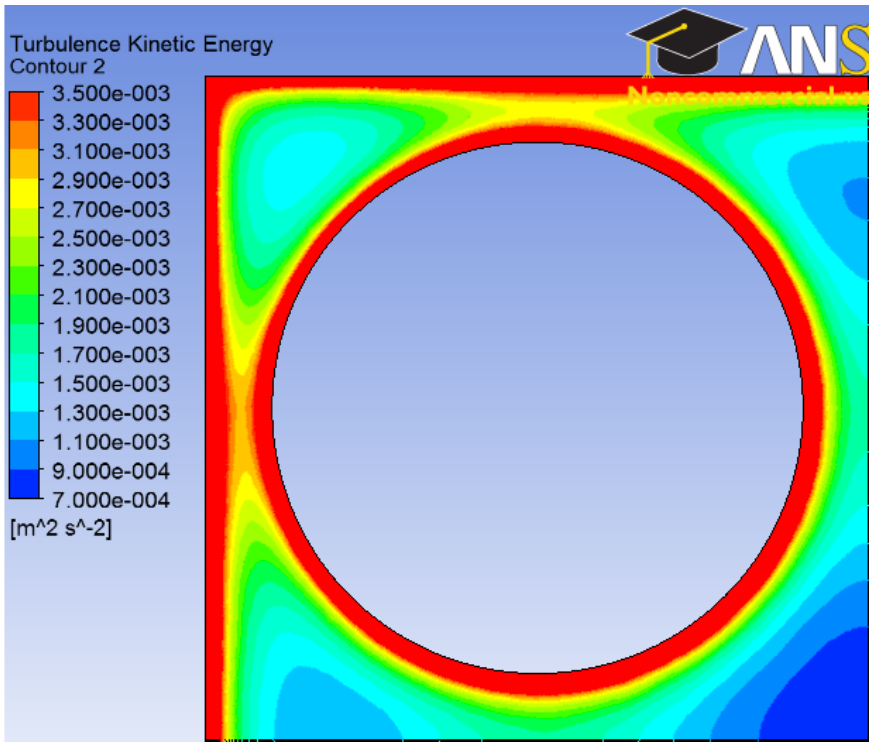

Figure 3-19. Contour graph of the turbulence kinetic energy using CFX for the 2x2 bundle using a smaller scale to show the azimuthal distribution.

Figure 3-20 shows the reported turbulence kinetic energy along the x-axis, and Figure 3-21 illustrates the same graph for the CFX results. The location of the x-axis can be found in Figure 3-17. These figures demonstrate that CFX predicts an order of magnitude less turbulence than measured in the experiment. This small level of turbulence implies the flow is almost laminar. Figure 3-22 shows that the turbulence kinetic energy is an appropriate value at the inlet, as specified, but declines an order of magnitude with increasing height.

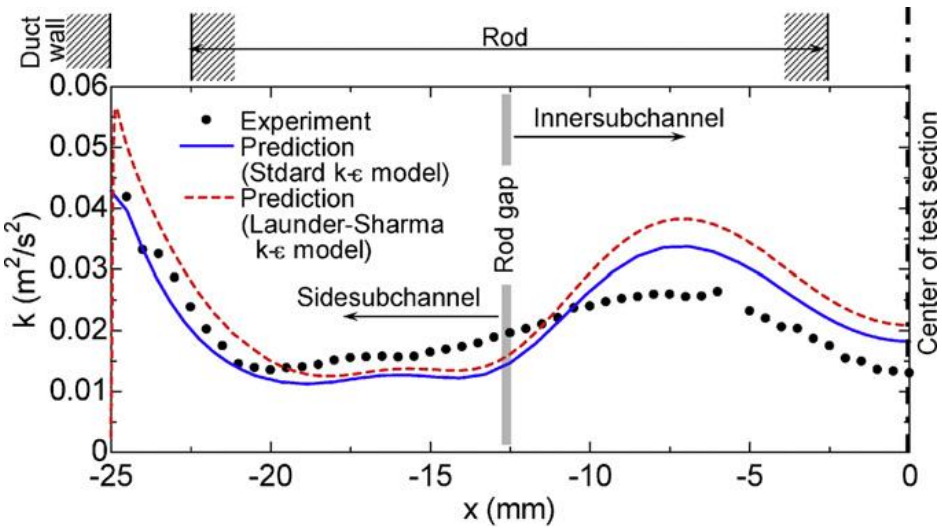

Figure 3-20. Graph of turbulence kinetic energy along the x-axis from the experiment [8].

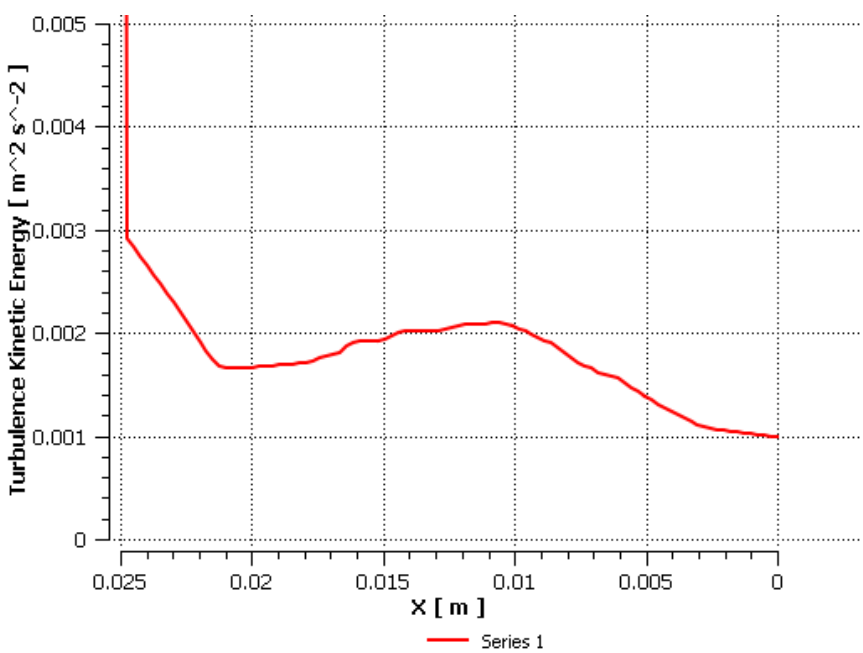

Figure 3-21. Graph of turbulence kinetic energy along the x-axis from CFX.

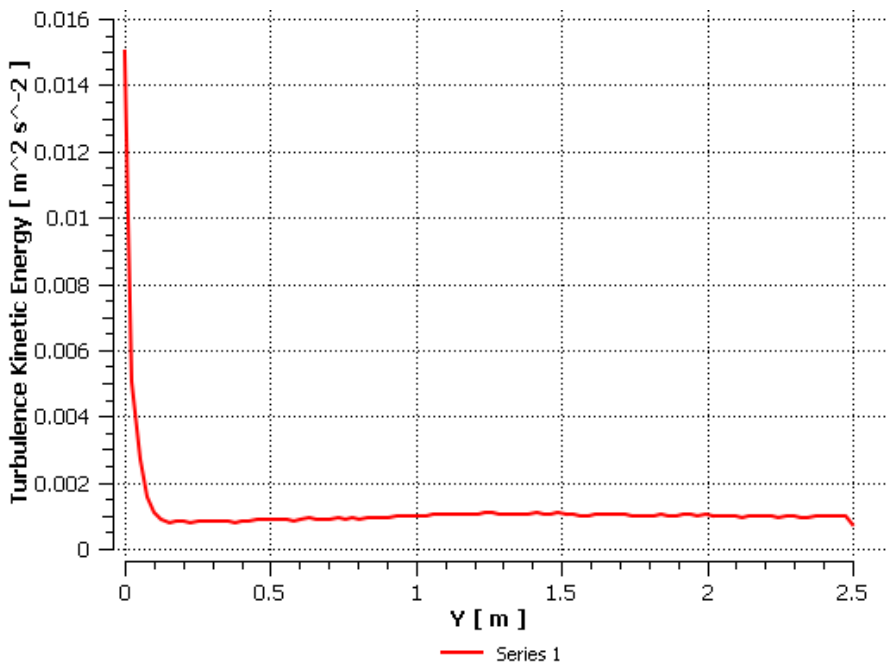

Figure 3-22. Axial distribution of turbulence kinetic energy in the center of the bundle.

Since the results for the k-epsilon model were poor, additional turbulence models were tested. The RSM model predicted about the same turbulence kinetic energy as the k-epsilon model did. The k-omega model provided slightly better results, but the turbulence kinetic energy was still very close to the laminar flow regime. The turbulence kinetic energy for the k-omega model is shown in Figure 3-23 below. This graph shows the correct expected trend, but the value is much too small. These models were also tested using the incompressible flow assumption, but the results were no different.

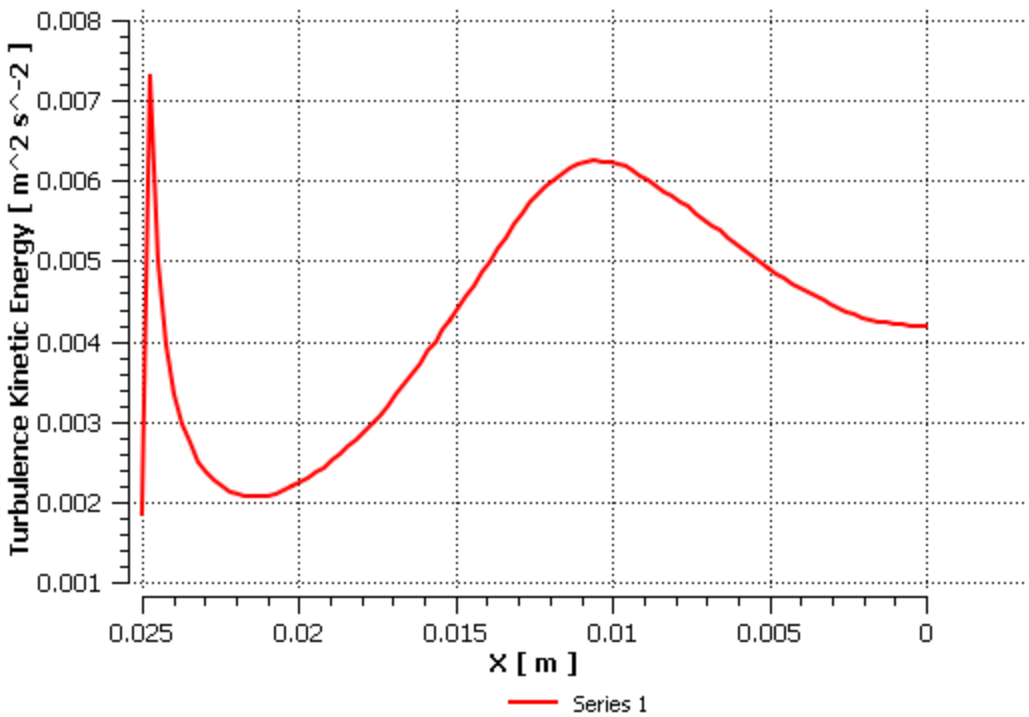

Figure 3-23. Turbulence kinetic energy along the x-axis using the k-omega turbulence model for the 2x2 bundle.

CFX under-predicted turbulence kinetic energy and eddy viscosity by about an order of magnitude, using different turbulence models. These terms were low enough to be in the laminar flow range, but Reynolds numbers corresponding to the computed velocities were greater than 25000, meaning the flow should be very turbulent. Despite the inability to predict turbulence kinetic energy, the predicted axial velocity was close to the experimental data. Hosokawa [8] shows that his CFD results, using Open FOAM, were comparable to the experimental data, so the CFX results would need further analysis for this particular bundle.

A quick analysis using a coarse mesh with about 1.6 million elements was performed for this bundle in order to test the effects of the mesh size. This coarse mesh produced results for turbulence kinetic energy at the appropriate magnitude, shown in Figure 3-24 below. It also produced a better axial velocity profile, shown in Figure 3-25. It is unknown

why the coarse mesh produces better results, but this mesh size would need further testing to determine if it can produce an accurate representation of the bundle.

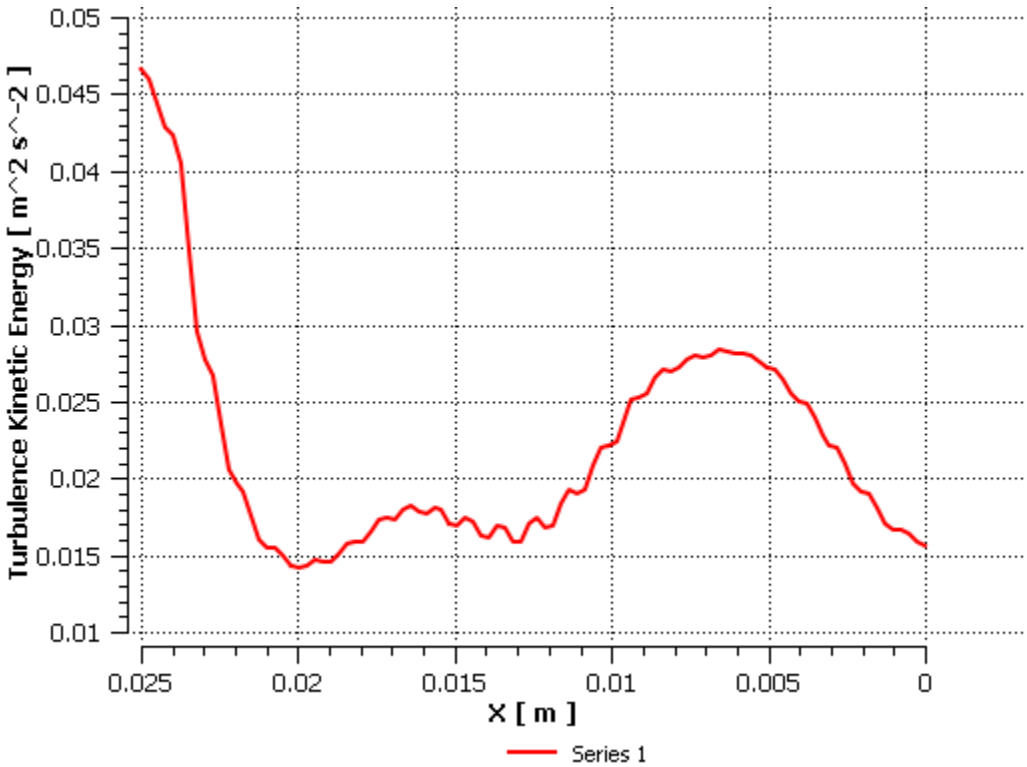

Figure 3-24. Turbulence kinetic energy along the x-axis for the coarse mesh.

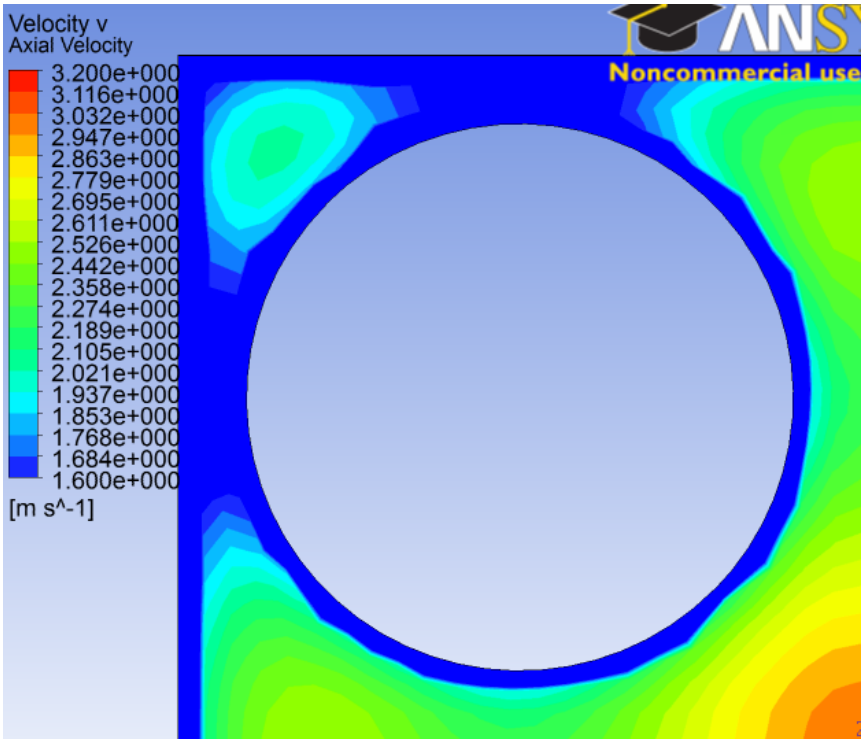

Figure 3-25. Contour graph of the axial velocity for 2x2 bundle using the coarse mesh.

While the fine mesh results from CFX were not promising, Yidong Xia [17] performed the same analysis using ANSYS FLUENT [18] with very accurate results. His simulated height was 1.5 meters, and the flow was assumed to be incompressible. The mesh is shown in Figure 3-26, and the total number of elements in the mesh is about 1.8 million. As seen in Figure 3-27, the turbulence kinetic energy distribution is similar to the experimental data in Figure 3-20 when using the k-omega turbulence model. Figure 3-28 shows a graph of the turbulence kinetic energy along the x-axis using different turbulence models, including the results from the experimenters. Using the standard k-ε model in FLUENT over predicts the turbulence kinetic energy, but using an enhanced wall treatment model makes the k-ε model more accurate, though the k-omega model more closely predicts the experimental results than either of these models.

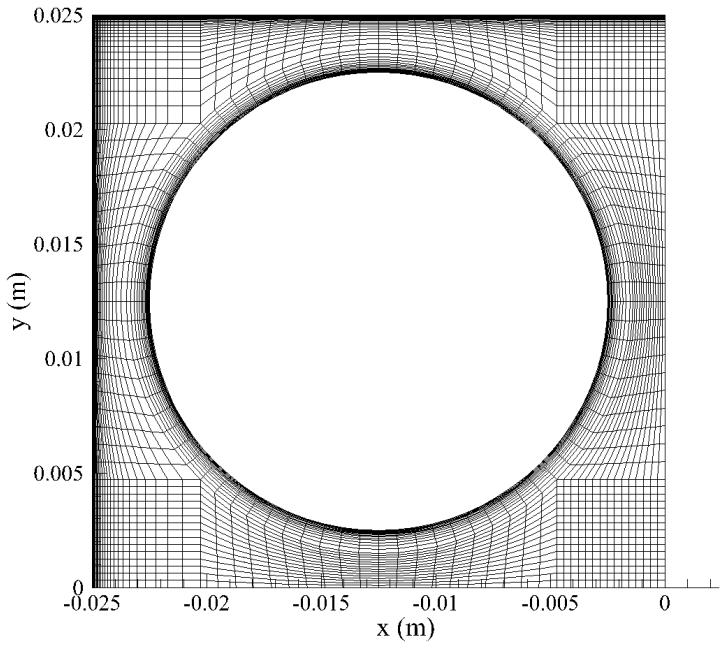

Figure 3-26. Mesh diagram for 2x2 bundle used in FLUENT [17].

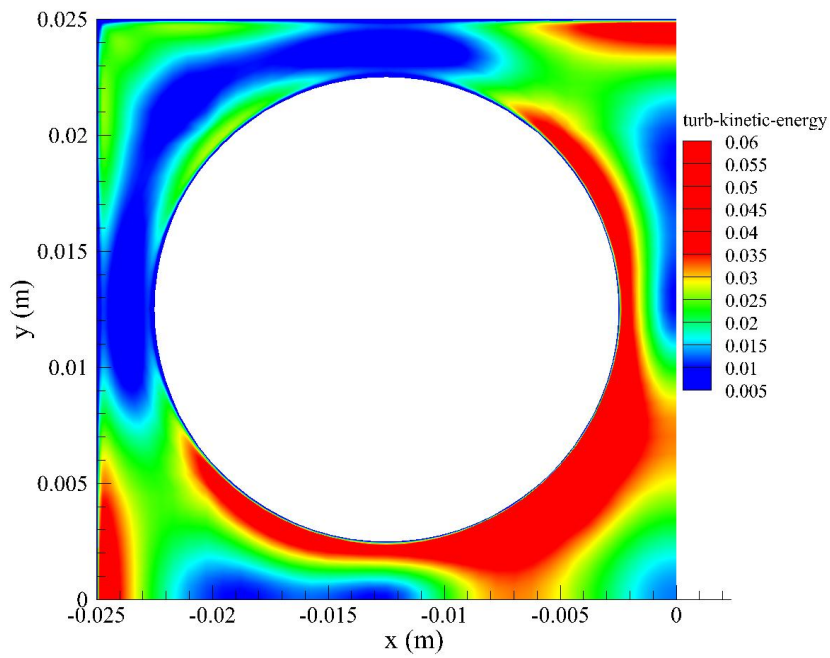

Figure 3-27. Contour graph of the turbulence kinetic energy using FLUENT with the k-omega turbulence model for the 2x2 bundle [17].

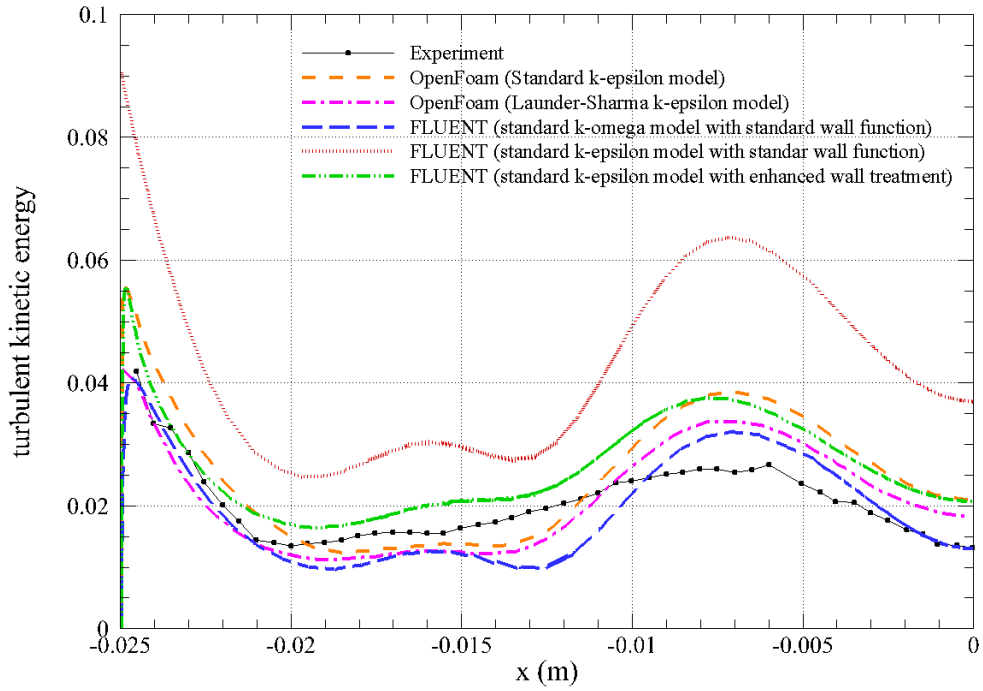

Figure 3-28. Graph of turbulence kinetic energy along the x-axis from FLUENT [17].

4 Comparison of a Typical PWR 17x17 bundle

A simple comparison between CFX and COBRA was done on a typical PWR 17x17 bundle; the COBRA input files were provided in the COBRA-EN package [6]. A diagram of a quarter of the bundle is shown in Figure 4-1, which includes a numbering scheme for an eighth of the bundle and which rods were heated and unheated. The rods were numbered in the same fashion as the channels. Table 4-1 illustrates the conditions and geometry for the bundle, and Figure 4-2 shows the actual power distribution for the hot and cold rods. The power for each rod was averaged to produce a constant axial heat rate, and then similar values of heat rate were grouped into one of seven heat rate groups. The default bundle heat input led to some degree of subcooled boiling. As it was desired to have a fully single phase bundle for comparison to CFX, the heat rate of each group was reduced to ensure the bundle remained entirely single phase. The final values are shown in Table 4-2.

Table 4-1. Conditions and geometry of the 17x17 bundle.

Pressure (psia)	Inlet Enthalpy (Btu/lbm)	Average Mass Flux (lbm/hr-ft^2)	Diameter (in)	Pitch (in)	Rod to Wall (in)	Rod to Rod (in)	Height (ft)
2163	559	2.0E+06	0.374	0.4704	0.2834	0.096	14

Table 4-2. Heat rate groups.

Group	Linear Heat Rate (BTU/hr-ft)
1	7323.890234
2	7637.211741
3	7833.037683
4	8028.863625
5	8224.689567
6	8420.515509
7	8616.341451

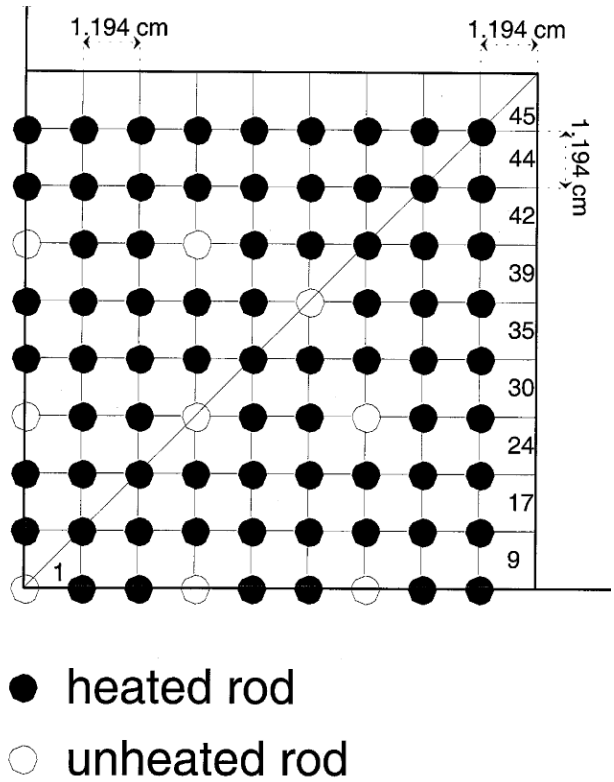

Figure 4-1. Diagram of the upper right quadrant of the 17x17 bundle.

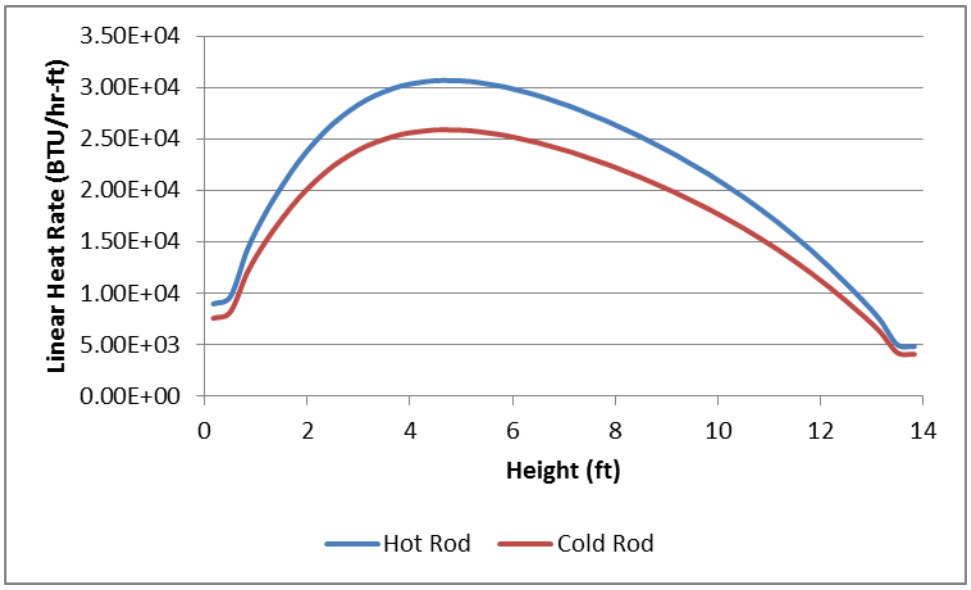

Figure 4-2. Initial power distribution for the 17x17 bundle.

This bundle was run using the k-epsilon and the Speziale, Sarkar, and Gatski [19] Reynolds stress turbulence models. The COBRA-EN results were used as a reference. This bundle has no spacer grids, so the inaccuracies in COBRA-EN associated with them are not present.

The figures below show the results of these simulations. The same two turbulent mixing models were used in COBRA-EN as was used for the 4x4 bundle. "COBRA-B" refers to the varying mixing coefficient correlation, while "COBRA" refers to the default, constant mixing coefficient correlation. Figure 4-3 illustrates the axial enthalpy distribution for the hot channel. The two turbulence models in CFX produce identical results. The enthalpy prediction in CFX begins larger than the COBRA-EN prediction, but they converge slightly with increasing height. These results show nearly the same exit enthalpy, which is promising for calculating thermal limits.

Figure 4-4 shows the axial temperature distribution on the hot rod and Figure 4-5 shows the axial heat transfer coefficient on the hot rod. The two turbulent mixing models in COBRA-EN give the same results, with differences observed between the two CFX turbulence models. The slope of the temperature distribution is greater for the RSM model than for the k-ε model, which may be because of the large dissimilarity in the heat transfer coefficient predicted by the two turbulence models. The k-ε model significantly over-predicts the heat transfer coefficient, by about a factor of 2. This over-prediction would cause the temperature of the rod to be under-predicted, which is seen in the results. The RSM model is clearly more accurate than the k-ε model when compared to COBRA-EN for these parameters, which is expected since the RSM model is a transport model while the k-ε model is based on the assumption that Reynolds stresses are proportional to the average velocity gradients [9]. These results show that CFX can predict axial wall temperature and heat transfer coefficient distributions with good accuracy as compared to COBRA-EN for a typical 17x17 bundle when using the RSM turbulence model.

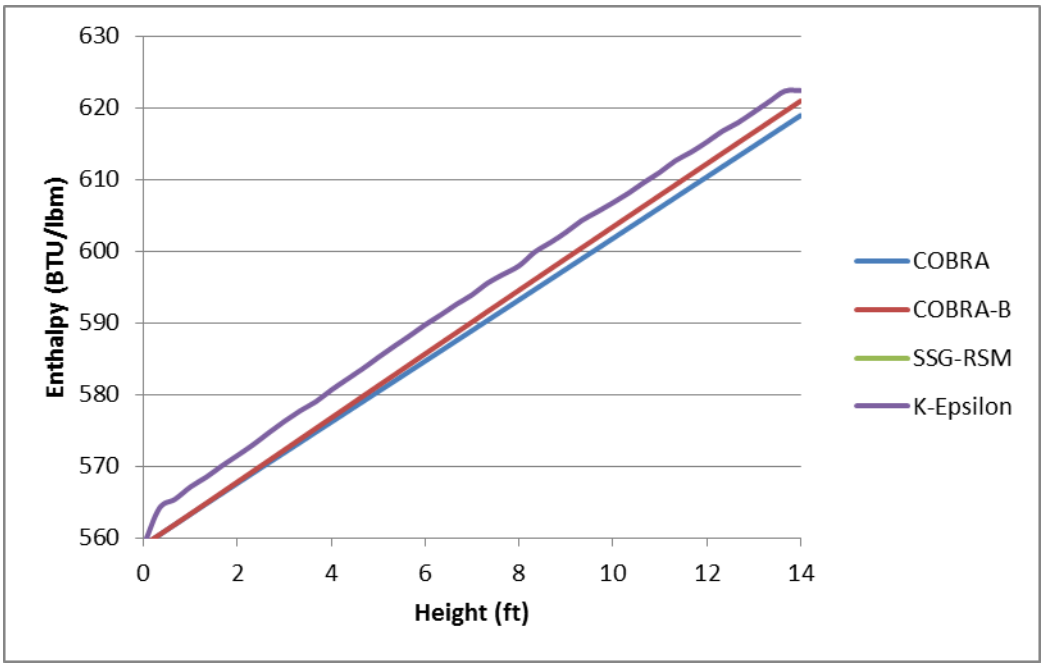

Figure 4-3. Axial enthalpy distribution in the hot channel (#10) for the 17x17 bundle.

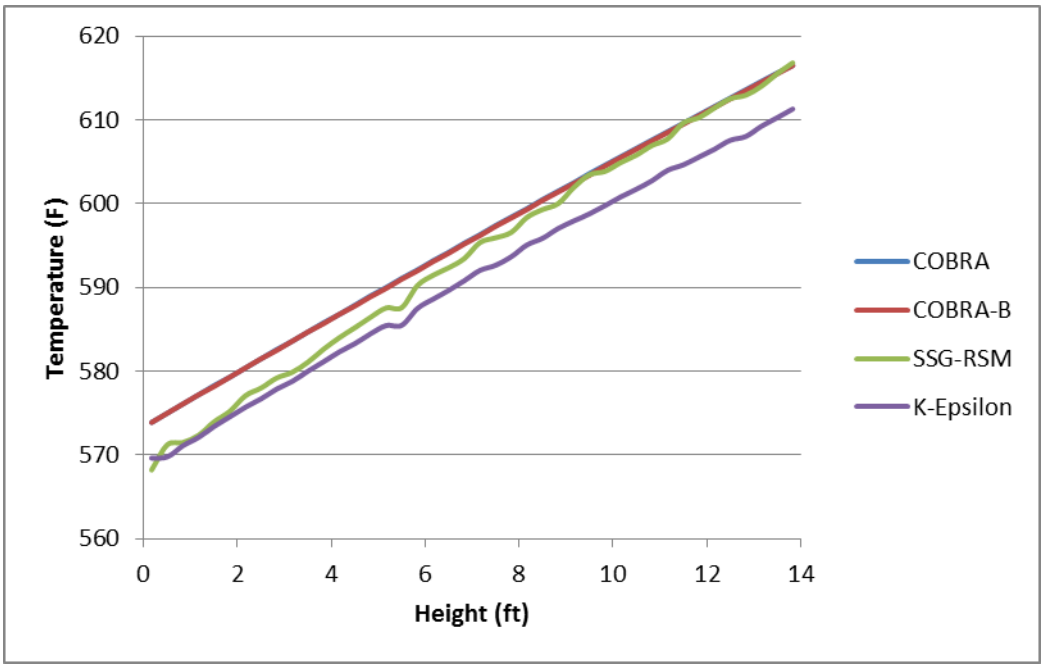

Figure 4-4. Axial temperature distribution on the hot rod (#3) for the 17x17 bundle.

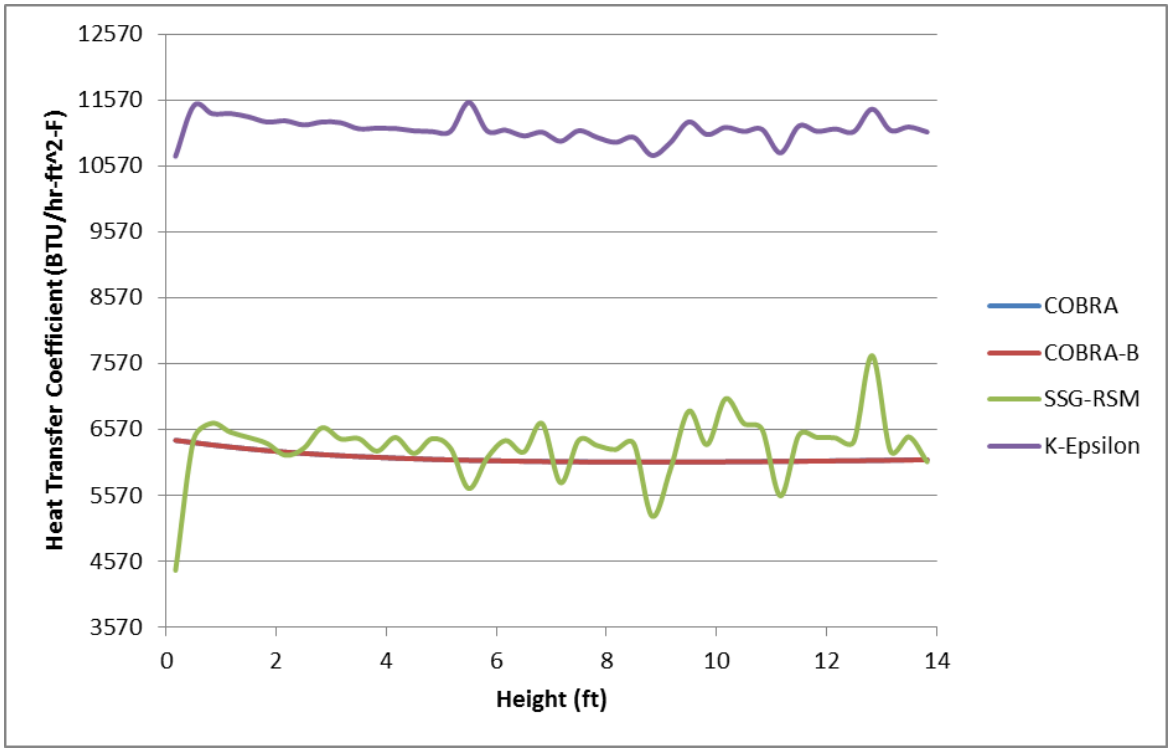

Figure 4-5. Axial heat transfer coefficient distribution on the hot rod for the 17x17 bundle.

5 Conclusions and Future Work

5.1 Conclusions

The 4x4 bundle results indicate that CFX predicts the average exit enthalpy very well when using a fine mesh. However, it is less accurate in predicting the exit enthalpy of individual subchannels. This lack of accuracy for the individual subchannels could result from CFX predicting a different temperature distribution than was found in the experiment. It could also result from measurement errors in the experiment, since the differences are rather small.

The 5x5 bundle results demonstrate that CFX predicts the turbulent mixing coefficient poorly for the given geometry. The mixing coefficients determined based on the CFX results differed by a factor of two to four compared to the mixing coefficients determined in the experiment. This error could be due to the use of a different version of the COBRA code, but it is unlikely to cause such large deviation. Another source of error is the spacer grids themselves, since their geometry was not given. A minor perturbation in the size of the spacer grids could have large mixing implications. The mixing coefficient is strongly dependent on exit enthalpy, which could be an additional source of error in determining the mixing coefficient. A 1-3% variation in exit enthalpy could lead to a variation in the mixing coefficient by a factor of two to four. One would thus conclude that this method is a poor method of comparison. These results also illustrate that a large variation in the mixing coefficient will not significantly alter the exit enthalpy, which leads one to believe that turbulent mixing does not have a large effect on the exit enthalpy distribution.

The 2x2 bundle results are rather disconcerting for the fine mesh. They indicate the turbulence kinetic energy is predicted poorly in CFX using the fine mesh with multiple turbulence models. The turbulence kinetic energy predicted in CFX is about an order of magnitude smaller than in the experiment, which is almost in the laminar flow regime. This issue seems to stem from mesh size in CFX, since the coarse mesh results show a good

agreement with the experimental data. Additional analysis should be performed on different mesh sizes and types to ensure the best results. While the CFX results varied depending on mesh sizing, FLUENT provided an accurate prediction when using the standard k-omega turbulence model and when using the k-ε turbulence model with enhanced wall treatment.

The 17x17 results demonstrate that CFX predicts the axial fluid enthalpy and wall temperature distributions closely in line with COBRA-EN, with the RSM turbulence model providing better predictions than the k-ε turbulence model. It also illustrates the k-epsilon model over-predicts the heat transfer coefficient as compared to COBRA-EN and the RSM turbulence model. Perhaps a k-ε model using a modified wall treatment could predict the heat transfer coefficient with better accuracy, since the standard model is not very accurate in the near wall region [9].

Based on the results presented in this paper, the methods of ANSYS CFX make acceptable predictions for flow and thermal properties, but make poor predictions for mixing and turbulence for the given geometries when using a fine mesh. Using COBRA-EN as the reference, CFX predicts the axial distributions of the thermal properties in the compared channels accurately. It is unknown why CFX predicts the turbulence properties poorly for the 2x2 bundle geometry with the fine mesh, while making more accurate predictions of the turbulence kinetic energy using a coarse mesh. Further testing should be performed on varying mesh sizes to determine why the CFX results were not accurate when using the fine mesh, and what sizes would produce the best results. There was limited data with which to compare flow and thermal properties, so finding or producing more data would aid in determining the accuracy of these codes. Although CFX needs further experimentation, ANSYS FLUENT was shown to provide accurate predictions for turbulence in the 2x2 bundle geometry with the use of the k-omega turbulence model and a modified k-epsilon model.

5.2 Future Work

The next steps in this process would be to consider other CFD codes, different meshes, and various turbulence models. There are many other CFD codes that could

potentially predict flow in rod bundles better than CFX. Examples of these codes were found in the literature: Hosokawa [8] used Open FOAM with good accuracy, Connor [9] developed a code starting from Star CD, and others used FLUENT. Their comparisons of experimental data to their CFD codes yielded good results, so those codes could potentially perform better than CFX for rod bundles. The mesh used in this analysis was a fine, mostly tetrahedral mesh. Other mesh types or sizes could be explored, such as a hex-dominant mesh or changing the meshing near walls, which may provide better results. Most of the widely used turbulence models available were tested, such as k-epsilon, Reynolds stress, and k-omega. There may be other turbulence models that are more suited to predicting turbulence in rod bundles, or using a certain special kind of the previously listed models may provide better results.

Since the nuclear industry is highly regulated, much additional testing and new experimentation will have to be done to completely validate specific CFD software for use in nuclear reactor thermal-hydraulic simulations. Much work is being done on this topic, as can be seen by the amount of recently published papers. If CFD can be proven to be accurate for rod bundles, then the industry can make the transition from the pseudo three dimensional subchannel methods approach to a fully three dimensional approach, allowing much greater detail in the solution. Having more detailed information would allow greater understanding of the thermal-hydraulics in the nuclear reactor, allowing for better reactor and fuel designs both from a safety and applicability standpoint.

Bibliography

[1] D. Rowe and B. Johnson, "Implications concerning rod bundle crossflow mixing based on measurements of turbulent flow structure," *Int. J. Heat Mass Transfer,* vol. 17, pp. 407-419, 1974.

[2] F. S. Castellana, W. T. Adams and J. E. Casterline, "Single-phase subchannel mixing in a simulated nuclear fuel assembly," *Nuclear Engineering and Design,* vol. 26, no. 2, pp. 242-249, 1974.

[3] K. Rehme, "The structure of turbulence in rod bundles and the implications on natural mixing between the subchannels," *Int. J. Heat Mass Transfer,* vol. 35, no. 2, pp. 567-581, 1992.

[4] S. V. Moeller, "Single-phase turbulent mixing in rod bundles," *Experimental Thermal and Fluid Science,* vol. 5, pp. 26-33, 1992.

[5] D. Rowe and C. Angle, Crossflow mixing between parallel flow channels during boiling, Pacific Northwest Laboratory, 1967.

[6] D. Basile, M. Beghi, R. Chierici, E. Salina and E. Brega, "COBRA-EN, An upgraded version of the COBRA-3C/MIT code for thermal-hydraulic transient analysis of light water reactor fuel assemblies and cores," Radiation Safety Information Computational Center, Oak Ridge National Lab, 1999.

[7] H.-Y. Jeong, K.-S. Ha, Y.-M. Kwon, Y.-B. Lee and D. Hahn, "A dominant geometrical parameter affecting the tubrulent mixing rate in rod bundles," *International Journal of Heat and Mass Transfer,* vol. 50, pp. 908-918, 2007.

[8] S. Hosokawa, T. Yamamoto, J. Okajima and A. Tomiyama, "Measurements of turbulent flows in a 2x2 bundle," *Nuclear Engineering and Design,* vol. doi:10.1016/j.nucengdes.2011.11.035, 2011.

[9] S. B. Pope, Turbulent Flows, Cambridge: Cambridge University Press, 2000.

[10] M. E. Conner, E. Baglietto and A. M. Elmahdi, "CFD methodology and validation for single-phase flow in PWR fuel assemblies," *Nuclear Engineering and Design,* vol. 240, pp. 2088-2095, 2010.

[11] C. Liu and Y. Ferng, "Numerically simulating the thermal-hydraulic characteristics within the fuel rod bundle using CFD methodology," *Nuclear Engineering and Design,* vol. 240, pp. 3078-3086, 2010.

[12] ANSYS Inc., "ANSYS CFX-solver theory guide," ANSYS CFX Release 12.0, 2009.

[13] ANSYS Academic Research, Release 13.0, CFX-Solver, ANSYS, Inc., 2010.

[14] F. S. Castellana and J. E. Casterline, "Subchannel flow and enthalpy distributions at the exit of a typical nuclear fuel core geometry," *Nuclear Engineering and Design,* vol. 22, no. 1, pp. 3-18, 1972.

[15] D. Rowe, "A digital computer program for thermal-hydraulic subchannel analysis of rod bundle nuclear fuel elements," BNWL-1229, 1970.

[16] M. Raffel, C. E. Willert, S. T. Wereley and J. Kompenhans, Particle Image Velocimetry: A Practical Guide, New York: Springer, 2007.

[17] Y. Xia, Interviewee, *FLUENT results for the 2x2 bundle.* [Interview]. May 2012.

[18] ANSYS Academic Research, Release 13.0, FLUENT-Solver, ANSYS, Inc., 2010.

[19] C. G. Speziale, S. Sarkar and T. B. Gatski, "Modelling the pressure-strain correlation of turbulence: an invariant dynamical systems approach," *J. Fluid Mech.,* vol. 227, pp. 245-272, 1991.

APPENDICES

Appendix A: Turbulence Models

A.1 K-epsilon turbulence model

The k-epsilon turbulence model is a two-equation turbulent-viscosity model, which relies on the eddy viscosity assumption [17]. This assumption is that the Reynolds stresses are proportional to the mean velocity gradients, and are given by the following:

$$\rho\langle u_i u_j\rangle = \frac{2}{3}\rho k\delta_{ij} - \mu_T\left(\frac{\delta\langle U_i\rangle}{\delta x_j} + \frac{\delta\langle U_j\rangle}{\delta x_i}\right) \qquad \text{A.1}$$

where μ_T is the eddy viscosity or turbulent viscosity. It is the most broadly used turbulence model and has a wide range of applicability. The two equations solved in the k-ε model are for turbulence kinetic energy, k, and the rate of dissipation, ε. The k equation is essentially an exact equation and is as follows:

$$\frac{\bar{D}k}{\bar{D}t} = \nabla\cdot\left(\frac{\mu_T}{\rho\sigma_k}\nabla k\right) + P - \varepsilon \qquad \text{A.2}$$

where P is the production term and σ_k is a constant. The ε equation is mostly empirical and is as follows:

$$\frac{\bar{D}\varepsilon}{\bar{D}t} = \nabla\cdot\left(\frac{\mu_T}{\rho\sigma_\varepsilon}\nabla\varepsilon\right) + C_{\varepsilon 1}\frac{P\varepsilon}{k} - C_{\varepsilon 2}\frac{\varepsilon^2}{k} \qquad \text{A.3}$$

where σ_ε, $C_{\varepsilon 1}$ and $C_{\varepsilon 2}$ are constants. An additional equation used to specify the eddy viscosity is as follows:

$$\mu_T = \frac{\rho C_\mu k^2}{\varepsilon} \qquad \text{A.4}$$

where C_μ is a constant. The standard values for the constants are as follows: $C_\mu = 0.09$, $C_{\varepsilon 1} = 1.44$, $C_{\varepsilon 2} = 1.92$, $\sigma_k = 1.0$, and $\sigma_\varepsilon = 1.3$. This model can be modified for different applications by modifying constants. The renormalization group method is an example of one of these modifications.

A.2 K-omega turbulence model

The k-ω model is the second most broadly used turbulence model [17]. It uses the same equation for k as the k-ε model, but uses a different second equation based on the turbulent frequency, ω. The k-ω model assumes the turbulent frequency is defined as $\omega = \frac{\varepsilon}{k}$. The equation for ω is as follows:

$$\frac{\bar{D}\omega}{\bar{D}t} = \nabla \cdot \left(\frac{\mu_T}{\rho\sigma_\omega}\nabla\omega\right) + C_{\omega 1}\frac{P\omega}{k} - C_{\omega 2}\omega^2 + \frac{2\mu_T}{\rho\sigma_\omega k}\nabla\omega \cdot \nabla k \qquad \text{A.5}$$

where $\sigma_\omega = 1$, $C_{\omega 1} = 0.44$, and $C_{\omega 2} = 0.92$. This model is better than the standard k-ε model in the near-wall region, and it takes into account the streamwise pressure gradients.

A.3 Reynolds stress turbulence model

The Reynolds stress model solves for the Reynolds stresses directly, so the eddy viscosity assumption is not necessary, making the model intrinsically more accurate than the above models [17]. The equations for the Reynolds stress model are as follows:

$$\frac{\bar{D}}{\bar{D}t}\langle u_i u_j\rangle + \frac{\partial}{\partial x_k}T_{kij} = \mathcal{P}_{ij} + R_{ij} - \varepsilon_{ij} \qquad \text{A.6}$$

$$\varepsilon_{ij} = 2v\,\langle\frac{\partial u_i}{\partial x_k}\frac{\partial u_j}{\partial x_k}\rangle \qquad \text{A.7}$$

$$R_{ij} = \langle\frac{P'}{\rho}\left(\frac{\partial u_i}{\partial x_j} + \frac{\partial u_j}{\partial x_i}\right)\rangle \qquad \text{A.8}$$

$$\mathcal{P}_{ij} = -\langle u_i u_k\rangle\frac{\partial\langle U_j\rangle}{\partial x_k} - \langle u_j u_k\rangle\frac{\partial\langle U_i\rangle}{\partial x_k} \qquad \text{A.9}$$

$$T_{kij} = T_{kij}^{(u)} + T_{kij}^{(p)} + T_{kij}^{(v)} \qquad \text{A.10}$$

$$T_{kij}^{(u)} = \langle u_i u_j u_k\rangle \qquad \text{A.11}$$

$$T_{kij}^{(v)} = -v\frac{\partial\langle u_i u_j\rangle}{\partial x_k} \qquad \text{A.12}$$

$$T_{kij}^{(p)} = \frac{1}{\rho}\langle u_i P'\rangle\delta_{jk} + \frac{1}{\rho}\langle u_j P'\rangle\delta_{ik} \qquad \text{A.13}$$

where T_{kij} is the Reynolds-stress flux, $\mathcal{P}_{ij}$ is the production tensor, R_{ij} is the pressure rate of strain tensor, ε_{ij} is the dissipation tensor, and P' is the pressure. Many models for the pressure rate of strain have been developed, each with varying applicability. The model used in this investigation was the SSG model proposed by Speziale, Sarkar, and Gatski [18].

Appendix B: COBRA-EN Input Files

B.1 4x4 Bundle Using the Varying Mixing Coefficient Correlation for Case 22

```
$ Three-equation model with homgeneous void model - Upflow solution
$2 IQP3  ISIN  ISOUT JTHMOD
    1    1    1    0
$3IPILE NCHANL NROD  NDX  NCTYP NGRID NGRIDT NODESF IGCON     IVEC2 NFUELT
    1   15    8   15    5    0    0    5    0    0    0    1
$4  DX(J)
  -0.3333
$5a NAXP
    15
$5b XTAB(J)
  0.166667
$5c QTAB(N,J)
 4.56338E+04 4.56338E+04 4.56338E+04 4.56338E+04 3.88732E+04 3.88732E+04
 3.88732E+04 3.88732E+04
  0.5
 4.56338E+04 4.56338E+04 4.56338E+04 4.56338E+04 3.88732E+04 3.88732E+04
 3.88732E+04 3.88732E+04
  0.83333
 4.56338E+04 4.56338E+04 4.56338E+04 4.56338E+04 3.88732E+04 3.88732E+04
 3.88732E+04 3.88732E+04
  1.16666
 4.56338E+04 4.56338E+04 4.56338E+04 4.56338E+04 3.88732E+04 3.88732E+04
 3.88732E+04 3.88732E+04
```

1.5
4.56338E+04 4.56338E+04 4.56338E+04 4.56338E+04 3.88732E+04 3.88732E+04
3.88732E+04 3.88732E+04
1.83332
4.56338E+04 4.56338E+04 4.56338E+04 4.56338E+04 3.88732E+04 3.88732E+04
3.88732E+04 3.88732E+04
2.16665
4.56338E+04 4.56338E+04 4.56338E+04 4.56338E+04 3.88732E+04 3.88732E+04
3.88732E+04 3.88732E+04
2.5
4.56338E+04 4.56338E+04 4.56338E+04 4.56338E+04 3.88732E+04 3.88732E+04
3.88732E+04 3.88732E+04
2.83331
4.56338E+04 4.56338E+04 4.56338E+04 4.56338E+04 3.88732E+04 3.88732E+04
3.88732E+04 3.88732E+04
3.16664
4.56338E+04 4.56338E+04 4.56338E+04 4.56338E+04 3.88732E+04 3.88732E+04
3.88732E+04 3.88732E+04
3.5
4.56338E+04 4.56338E+04 4.56338E+04 4.56338E+04 3.88732E+04 3.88732E+04
3.88732E+04 3.88732E+04
3.83330
4.56338E+04 4.56338E+04 4.56338E+04 4.56338E+04 3.88732E+04 3.88732E+04
3.88732E+04 3.88732E+04
4.16663
4.56338E+04 4.56338E+04 4.56338E+04 4.56338E+04 3.88732E+04 3.88732E+04
3.88732E+04 3.88732E+04
4.5
4.56338E+04 4.56338E+04 4.56338E+04 4.56338E+04 3.88732E+04 3.88732E+04
3.88732E+04 3.88732E+04
4.83329
4.56338E+04 4.56338E+04 4.56338E+04 4.56338E+04 3.88732E+04 3.88732E+04
3.88732E+04 3.88732E+04
$7 NCN NCC(L) GAPC(L) DISTC(L)
1 2 .0123 .0463 4 .0123 .0463

```
   2     3 .0123 .0463  5 .0111 .0463
   3    -3 .0123 .0463  6 .0111 .0463
   4     5 .0111 .0463  7 .0123 .0463
   5     6 .0111 .0463  8 .0111 .0463
   6    -6 .0111 .0463  9 .0111 .0463
   7     8 .0111 .0463 10 .0123 .0463
   8     9 .0111 .0463 11 .0111 .0463
   9    -9 .0111 .0463 12 .0111 .0463
  10    11 .0111 .0463 13 .0123 .0463
  11    12 .0111 .0463 14 .0111 .0463
  12   -12 .0111 .0463 15 .0111 .0463
  13    14 .0123 .0463  0
  14    15 .0123 .0463  0
  15   -15 .0123 .0463
   0     0
$8 NRN IDFUEL LR(L) PHI(L)
 1     1     1 .2500  2 .2500  4 .2500  5 .2500
 2     1     2 .2500  3 .2500  5 .2500  6 .2500
 3     1     4 .2500  5 .2500  7 .2500  8 .2500
 4     1     5 .2500  6 .2500  8 .2500  9 .2500
 5     1     7 .2500  8 .2500 10 .2500 11 .2500
 6     1     8 .2500  9 .2500 11 .2500 12 .2500
 7     1    10 .2500 11 .2500 13 .2500 14 .2500
 8     1    11 .2500 12 .2500 14 .2500 15 .2500
000
$10A N FRAC   CHAR         CHPW        CHPH
$Center
   1 1.000 1.16776E-03 1.10479E-01 1.10479E-01
$10B CDG(L) - single phase grid coefficients
$ 0.513
$10C JB(L)
$Edge
   1 1.000 8.97997E-04 1.01490E-01 5.52397E-02
$ 0.513
   2    4    7   10   14    0
```

```
$Corner
    1 1.000 4.09358E-04 7.38698E-02 2.76198E-02
$ 0.513
    1    13     0
$Center symmetry
    1 0.500 1.16776E-03 1.10479E-01 1.10479E-01
$ 0.513
    6     9    12
$Edge Symmetry
    1 0.500 8.97997E-04 1.01490E-01 5.52397E-02
$ 0.513
    3    15
$11 GRIDXL(I) IGRID(I)
$  0.05     1 .2167     1 .3833     1  0.55     1 .7167     1 .8833     1
$12A DFUEL   TCLAD        RFUEL     RCLAD       DROD
  0.034334   8.33E-4       642.0     405.0       0.035167
$12B KFUEL    CFUEL        KCLAD     CCLAD       HGAP
   2.0       0.058         8.80      0.058       1000.
$14 N1    N2     N3    N4    N5    N6    N7    N8   NHTC  ISAT
    3     0     1     1     0     1     1     0     1     0
$15 ABETA BBETA NBBC GK
 .0296 -0.10     0   0.0
$18 J4
    2
$20  J2    J3   JSLIP
    3     3
$22 IBC1  IBC2  IBC3  IBC4  IBC5  IBC6
    0     0     0     0     0     0
$26A KIJ FTM   SL   THETA
  0.5   0.0   0.5   0.0
$26B NCHF NCWC NUFC CGRID  NCPR  NTCPR RGE   FPRC SPACNG
    3     0     0   0.0     0     0    0.    0.    0.
$27ITRY NTRY FERROR WERRX DAMPP DAMPF HTCERR TERR ITRNSX ERRCON EPSP ISCHEM
    0     0    0.    0.    0.    0.  -.01    0.     0    0.    0.     1
$29 IH  HIN   GIN  PEXIT   DPS    IPS FNORM   CQ  GINBP BORIN  CQIN  HOUT
```

```
   0  172. 1.01  1200.   0.0     0   1.0    0.     0    0.     0    0.
$30A TTIME NDT  NSLUG
  0.     0     0
$32 NP              NQ    NBOR
   0     0     0     0     0
$36 NSKIPX NSKIPT NOUT NPCHAN NPROD NPNODE NPLOT
   0     0     3     0     0     0     0
$37 Channel IDs to be printed         (i=1, NPCHAN)
$     1     9    26    35
$38 Rod IDs to be printed (i=1, NPROD)
$     1     6     9    24    32    36
$EOD
```

B.2 5x5 Bundle with Spacer Grids Using the Varying Mixing Coefficient Correlation for Case 1

```
$ Three-equation model with homgeneous void model - Upflow solution
$2 IQP3  ISIN  ISOUT JTHMOD
   1     1     1     0
$3IPILE NCHANL NROD  NDX  NCTYP NGRID NGRIDT NODESF IGCON     IVEC2 NFUELT
   1    36    25    18     3     4     1     5     0     0     0     1
$4  DX(J)
  -0.3333
$5a NAXP
   18
$5b XTAB(J)
  0.166667
$5c QTAB(N,J)
 2.16540E+04 2.16540E+04 2.16540E+03 2.16540E+03 2.16540E+03 2.16540E+04
 2.16540E+04 2.16540E+03 2.16540E+03 2.16540E+03 2.16540E+04 2.16540E+04
 2.16540E+03 2.16540E+03 2.16540E+03 2.16540E+04 2.16540E+04 2.16540E+03
 2.16540E+03 2.16540E+03 2.16540E+04 2.16540E+04 2.16540E+03 2.16540E+03
 2.16540E+03
  0.5
 2.16540E+04 2.16540E+04 2.16540E+03 2.16540E+03 2.16540E+03 2.16540E+04
```

2.16540E+04 2.16540E+03 2.16540E+03 2.16540E+03 2.16540E+04 2.16540E+04
2.16540E+03 2.16540E+03 2.16540E+03 2.16540E+04 2.16540E+04 2.16540E+03
2.16540E+03 2.16540E+03 2.16540E+04 2.16540E+04 2.16540E+03 2.16540E+03
2.16540E+03
0.83333
2.16540E+04 2.16540E+04 2.16540E+03 2.16540E+03 2.16540E+03 2.16540E+04
2.16540E+04 2.16540E+03 2.16540E+03 2.16540E+03 2.16540E+04 2.16540E+04
2.16540E+03 2.16540E+03 2.16540E+03 2.16540E+04 2.16540E+04 2.16540E+03
2.16540E+03 2.16540E+03 2.16540E+04 2.16540E+04 2.16540E+03 2.16540E+03
2.16540E+03
1.16666
2.16540E+04 2.16540E+04 2.16540E+03 2.16540E+03 2.16540E+03 2.16540E+04
2.16540E+04 2.16540E+03 2.16540E+03 2.16540E+03 2.16540E+04 2.16540E+04
2.16540E+03 2.16540E+03 2.16540E+03 2.16540E+04 2.16540E+04 2.16540E+03
2.16540E+03 2.16540E+03 2.16540E+04 2.16540E+04 2.16540E+03 2.16540E+03
2.16540E+03
1.5
2.16540E+04 2.16540E+04 2.16540E+03 2.16540E+03 2.16540E+03 2.16540E+04
2.16540E+04 2.16540E+03 2.16540E+03 2.16540E+03 2.16540E+04 2.16540E+04
2.16540E+03 2.16540E+03 2.16540E+03 2.16540E+04 2.16540E+04 2.16540E+03
2.16540E+03 2.16540E+03 2.16540E+04 2.16540E+04 2.16540E+03 2.16540E+03
2.16540E+03
1.83332
2.16540E+04 2.16540E+04 2.16540E+03 2.16540E+03 2.16540E+03 2.16540E+04
2.16540E+04 2.16540E+03 2.16540E+03 2.16540E+03 2.16540E+04 2.16540E+04
2.16540E+03 2.16540E+03 2.16540E+03 2.16540E+04 2.16540E+04 2.16540E+03
2.16540E+03 2.16540E+03 2.16540E+04 2.16540E+04 2.16540E+03 2.16540E+03
2.16540E+03
2.16665
2.16540E+04 2.16540E+04 2.16540E+03 2.16540E+03 2.16540E+03 2.16540E+04
2.16540E+04 2.16540E+03 2.16540E+03 2.16540E+03 2.16540E+04 2.16540E+04
2.16540E+03 2.16540E+03 2.16540E+03 2.16540E+04 2.16540E+04 2.16540E+03
2.16540E+03 2.16540E+03 2.16540E+04 2.16540E+04 2.16540E+03 2.16540E+03
2.16540E+03
2.5

2.16540E+04 2.16540E+04 2.16540E+03 2.16540E+03 2.16540E+03 2.16540E+04
2.16540E+04 2.16540E+03 2.16540E+03 2.16540E+03 2.16540E+04 2.16540E+04
2.16540E+03 2.16540E+03 2.16540E+03 2.16540E+04 2.16540E+04 2.16540E+03
2.16540E+03 2.16540E+03 2.16540E+04 2.16540E+04 2.16540E+03 2.16540E+03
2.16540E+03
2.83331
2.16540E+04 2.16540E+04 2.16540E+03 2.16540E+03 2.16540E+03 2.16540E+04
2.16540E+04 2.16540E+03 2.16540E+03 2.16540E+03 2.16540E+04 2.16540E+04
2.16540E+03 2.16540E+03 2.16540E+03 2.16540E+04 2.16540E+04 2.16540E+03
2.16540E+03 2.16540E+03 2.16540E+04 2.16540E+04 2.16540E+03 2.16540E+03
2.16540E+03
3.16664
2.16540E+04 2.16540E+04 2.16540E+03 2.16540E+03 2.16540E+03 2.16540E+04
2.16540E+04 2.16540E+03 2.16540E+03 2.16540E+03 2.16540E+04 2.16540E+04
2.16540E+03 2.16540E+03 2.16540E+03 2.16540E+04 2.16540E+04 2.16540E+03
2.16540E+03 2.16540E+03 2.16540E+04 2.16540E+04 2.16540E+03 2.16540E+03
2.16540E+03
3.5
2.16540E+04 2.16540E+04 2.16540E+03 2.16540E+03 2.16540E+03 2.16540E+04
2.16540E+04 2.16540E+03 2.16540E+03 2.16540E+03 2.16540E+04 2.16540E+04
2.16540E+03 2.16540E+03 2.16540E+03 2.16540E+04 2.16540E+04 2.16540E+03
2.16540E+03 2.16540E+03 2.16540E+04 2.16540E+04 2.16540E+03 2.16540E+03
2.16540E+03
3.83330
2.16540E+04 2.16540E+04 2.16540E+03 2.16540E+03 2.16540E+03 2.16540E+04
2.16540E+04 2.16540E+03 2.16540E+03 2.16540E+03 2.16540E+04 2.16540E+04
2.16540E+03 2.16540E+03 2.16540E+03 2.16540E+04 2.16540E+04 2.16540E+03
2.16540E+03 2.16540E+03 2.16540E+04 2.16540E+04 2.16540E+03 2.16540E+03
2.16540E+03
4.16663
2.16540E+04 2.16540E+04 2.16540E+03 2.16540E+03 2.16540E+03 2.16540E+04
2.16540E+04 2.16540E+03 2.16540E+03 2.16540E+03 2.16540E+04 2.16540E+04
2.16540E+03 2.16540E+03 2.16540E+03 2.16540E+04 2.16540E+04 2.16540E+03
2.16540E+03 2.16540E+03 2.16540E+04 2.16540E+04 2.16540E+03 2.16540E+03
2.16540E+03

4.5

2.16540E+04 2.16540E+04 2.16540E+03 2.16540E+03 2.16540E+03 2.16540E+04
2.16540E+04 2.16540E+03 2.16540E+03 2.16540E+03 2.16540E+04 2.16540E+04
2.16540E+03 2.16540E+03 2.16540E+03 2.16540E+04 2.16540E+04 2.16540E+03
2.16540E+03 2.16540E+03 2.16540E+04 2.16540E+04 2.16540E+03 2.16540E+03
2.16540E+03

4.83329

2.16540E+04 2.16540E+04 2.16540E+03 2.16540E+03 2.16540E+03 2.16540E+04
2.16540E+04 2.16540E+03 2.16540E+03 2.16540E+03 2.16540E+04 2.16540E+04
2.16540E+03 2.16540E+03 2.16540E+03 2.16540E+04 2.16540E+04 2.16540E+03
2.16540E+03 2.16540E+03 2.16540E+04 2.16540E+04 2.16540E+03 2.16540E+03
2.16540E+03

5.16662

2.16540E+04 2.16540E+04 2.16540E+03 2.16540E+03 2.16540E+03 2.16540E+04
2.16540E+04 2.16540E+03 2.16540E+03 2.16540E+03 2.16540E+04 2.16540E+04
2.16540E+03 2.16540E+03 2.16540E+03 2.16540E+04 2.16540E+04 2.16540E+03
2.16540E+03 2.16540E+03 2.16540E+04 2.16540E+04 2.16540E+03 2.16540E+03
2.16540E+03

5.5

2.16540E+04 2.16540E+04 2.16540E+03 2.16540E+03 2.16540E+03 2.16540E+04
2.16540E+04 2.16540E+03 2.16540E+03 2.16540E+03 2.16540E+04 2.16540E+04
2.16540E+03 2.16540E+03 2.16540E+03 2.16540E+04 2.16540E+04 2.16540E+03
2.16540E+03 2.16540E+03 2.16540E+04 2.16540E+04 2.16540E+03 2.16540E+03
2.16540E+03

5.83328

2.16540E+04 2.16540E+04 2.16540E+03 2.16540E+03 2.16540E+03 2.16540E+04
2.16540E+04 2.16540E+03 2.16540E+03 2.16540E+03 2.16540E+04 2.16540E+04
2.16540E+03 2.16540E+03 2.16540E+03 2.16540E+04 2.16540E+04 2.16540E+03
2.16540E+03 2.16540E+03 2.16540E+04 2.16540E+04 2.16540E+03 2.16540E+03
2.16540E+03

$7 NCN NCC(L) GAPC(L) DISTC(L)

1	2	.0096	.0469	7	.0096	.0469
2	3	.0096	.0469	8	.0118	.0469
3	4	.0096	.0469	9	.0118	.0469
4	5	.0096	.0469	10	.0118	.0469

```
 5    6 .0096 .0469 11 .0118 .0469
 6    0            12 .0096 .0469
 7    8 .0118 .0469 13 .0096 .0469
 8    9 .0118 .0469 14 .0118 .0469
 9   10 .0118 .0469 15 .0118 .0469
10   11 .0118 .0469 16 .0118 .0469
11   12 .0118 .0469 17 .0118 .0469
12    0            18 .0096 .0469
13   14 .0118 .0469 19 .0096 .0469
14   15 .0118 .0469 20 .0118 .0469
15   16 .0118 .0469 21 .0118 .0469
16   17 .0118 .0469 22 .0118 .0469
17   18 .0118 .0469 23 .0118 .0469
18    0            24 .0096 .0469
19   20 .0118 .0469 25 .0096 .0469
20   21 .0118 .0469 26 .0118 .0469
21   22 .0118 .0469 27 .0118 .0469
22   23 .0118 .0469 28 .0118 .0469
23   24 .0118 .0469 29 .0118 .0469
24    0            30 .0096 .0469
25   26 .0118 .0469 31 .0096 .0469
26   27 .0118 .0469 32 .0118 .0469
27   28 .0118 .0469 33 .0118 .0469
28   29 .0118 .0469 34 .0118 .0469
29   30 .0118 .0469 35 .0118 .0469
30    0            36 .0118 .0469
31   32 .0096 .0469
32   33 .0096 .0469
33   34 .0096 .0469
34   35 .0096 .0469
35   36 .0096 .0469
36    0
 0    0
$8 NRN IDFUEL LR(L) PHI(L)
 1    1    1 .2500  2 .2500  7 .2500  8 .2500
```

```
 2    1    2 .2500  3 .2500  8 .2500  9 .2500
 3    1    3 .2500  4 .2500  9 .2500 10 .2500
 4    1    4 .2500  5 .2500 10 .2500 11 .2500
 5    1    5 .2500  6 .2500 11 .2500 12 .2500
 6    1    7 .2500  8 .2500 13 .2500 14 .2500
 7    1    8 .2500  9 .2500 14 .2500 15 .2500
 8    1    9 .2500 10 .2500 15 .2500 16 .2500
 9    1   10 .2500 11 .2500 16 .2500 17 .2500
10    1   11 .2500 12 .2500 17 .2500 18 .2500
11    1   13 .2500 14 .2500 19 .2500 20 .2500
12    1   14 .2500 15 .2500 20 .2500 21 .2500
13    1   15 .2500 16 .2500 21 .2500 22 .2500
14    1   16 .2500 17 .2500 22 .2500 23 .2500
15    1   17 .2500 18 .2500 23 .2500 24 .2500
16    1   19 .2500 20 .2500 25 .2500 26 .2500
17    1   20 .2500 21 .2500 26 .2500 27 .2500
18    1   21 .2500 22 .2500 27 .2500 28 .2500
19    1   22 .2500 23 .2500 28 .2500 29 .2500
20    1   23 .2500 24 .2500 29 .2500 30 .2500
21    1   25 .2500 26 .2500 31 .2500 32 .2500
22    1   26 .2500 27 .2500 32 .2500 33 .2500
23    1   27 .2500 28 .2500 33 .2500 34 .2500
24    1   28 .2500 29 .2500 34 .2500 35 .2500
25    1   29 .2500 30 .2500 35 .2500 36 .2500
000
$10A N FRAC   CHAR         CHPW        CHPH
$Center
   1 1.000 1.22988E-03 1.10479E-01 1.10479E-01
$10B CDG(L) - single phase grid coefficients
 0.411
$10C JB(L)
$Edge
   1 1.000 7.88921E-04 1.02156E-01 5.52397E-02
 0.411
   2    3    4    5    7   12   13   18   19   24   25   30
```

```
   32    33    34    35     0
$Corner
    1 1.000 2.52379E-04 7.45365E-02 2.76198E-02
 0.411
    1     6    31    36     0
$11 GRIDXL(I) IGRID(I)
0.1667     1 0.375     1 0.583     1 0.792     1
$12A DFUEL   TCLAD        RFUEL     RCLAD       DROD
  0.034334   8.33E-4       642.0     405.0       0.035167
$12B KFUEL    CFUEL        KCLAD     CCLAD       HGAP
   2.0       0.058         8.80      0.058       1000.
$14 N1    N2     N3    N4    N5    N6    N7    N8   NHTC  ISAT
    3     0     1     1     0     1     1     0     1     0
$15 ABETA BBETA NBBC GK
.02835 -0.10     0   0.0
$18 J4
    2
$20  J2    J3   JSLIP
    3     3
$22 IBC1  IBC2  IBC3  IBC4  IBC5  IBC6
    0     0     0     0     0     0
$26A KIJ FTM   SL   THETA
  0.5   0.0   0.5   0.0
$26B NCHF NCWC NUFC CGRID  NCPR  NTCPR RGE   FPRC SPACNG
    3     0     0  0.0     0     0    0.    0.    0.
$27ITRY NTRY FERROR WERRX DAMPP DAMPF HTCERR TERR ITRNSX ERRCON EPSP ISCHEM
    0     0    0.    0.    0.    0.  -.01    0.     0    0.    0.     1
$29 IH  HIN   GIN  PEXIT   DPS    IPS FNORM   CQ  GINBP BORIN  CQIN  HOUT
    0  325.  1.55 1500.   0.0     0   1.0    0.     0    0.     0    0.
$30A TTIME NDT  NSLUG
   0.     0     0
$32 NP                NQ    NBOR
    0     0     0     0     0
$36 NSKIPX NSKIPT NOUT NPCHAN NPROD NPNODE NPLOT
    0     0     3     0     0     0     0
```

```
$37 Channel IDs to be printed        (i=1, NPCHAN)
$    1    9   26   35
$38 Rod IDs to be printed (i=1, NPROD)
$    1    6    9   24   32   36
$EOD
```

B.3 17x17 Bundle with Constant Axial Heat Flux Using the Varying Mixing Coefficient Correlation

```
$ Three-equation model with homgeneous void model - Upflow solution
$2 IQP3  ISIN  ISOUT JTHMOD
   1    1    1    0
$3IPILE NCHANL NROD  NDX  NCTYP NGRID NGRIDT NODESF IGCON    IVEC2 NFUELT
   1   45   45   42    4    0    0    5    0    0    0    1
$4  DX(J)
  -0.3333
$5 NAXP
   2
$6 XTAB(J)
 0.166667
$7 QTAB(N,J)
 0.00000E+00 8.61634E+03 8.61634E+03 0.00000E+00 8.61634E+03 8.61634E+03
 0.00000E+00 8.42052E+03 7.83304E+03 8.61634E+03 8.61634E+03 8.61634E+03
 8.61634E+03 8.61634E+03 8.61634E+03 8.42052E+03 7.83304E+03 8.61634E+03
 8.61634E+03 8.61634E+03 8.61634E+03 8.61634E+03 8.42052E+03 7.83304E+03
 0.00000E+00 8.61634E+03 8.61634E+03 0.00000E+00 8.42052E+03 7.83304E+03
 8.61634E+03 8.61634E+03 8.61634E+03 8.22469E+03 7.83304E+03 0.00000E+00
 8.42052E+03 8.22469E+03 7.83304E+03 8.22469E+03 8.02886E+03 7.63721E+03
 7.83304E+03 7.63721E+03 7.32389E+03
  13.83320
 0.00000E+00 8.61634E+03 8.61634E+03 0.00000E+00 8.61634E+03 8.61634E+03
 0.00000E+00 8.42052E+03 7.83304E+03 8.61634E+03 8.61634E+03 8.61634E+03
 8.61634E+03 8.61634E+03 8.61634E+03 8.42052E+03 7.83304E+03 8.61634E+03
 8.61634E+03 8.61634E+03 8.61634E+03 8.61634E+03 8.42052E+03 7.83304E+03
 0.00000E+00 8.61634E+03 8.61634E+03 0.00000E+00 8.42052E+03 7.83304E+03
```

8.61634E+03 8.61634E+03 8.61634E+03 8.22469E+03 7.83304E+03 0.00000E+00
8.42052E+03 8.22469E+03 7.83304E+03 8.22469E+03 8.02886E+03 7.63721E+03
7.83304E+03 7.63721E+03 7.32389E+03

$7 NCN NCC(L) GAPC(L) DISTC(L)

1	2	.0080	.0392			
2	3	.0080	.0392	10	.0080	.0392
3	4	.0080	.0392	11	.0080	.0392
4	5	.0080	.0392	12	.0080	.0392
5	6	.0080	.0392	13	.0080	.0392
6	7	.0080	.0392	14	.0080	.0392
7	8	.0080	.0392	15	.0080	.0392
8	9	.0080	.0392	16	.0080	.0392
9	0			17	.0236	.0392
10	11	.0080	.0392			
11	12	.0080	.0392	18	.0080	.0392
12	13	.0080	.0392	19	.0080	.0392
13	14	.0080	.0392	20	.0080	.0392
14	15	.0080	.0392	21	.0080	.0392
15	16	.0080	.0392	22	.0080	.0392
16	17	.0080	.0392	23	.0080	.0392
17	0			24	.0236	.0392
18	19	.0080	.0392			
19	20	.0080	.0392	25	.0080	.0392
20	21	.0080	.0392	26	.0080	.0392
21	22	.0080	.0392	27	.0080	.0392
22	23	.0080	.0392	28	.0080	.0392
23	24	.0080	.0392	29	.0080	.0392
24	0			30	.0236	.0392
25	26	.0080	.0392			
26	27	.0080	.0392	31	.0080	.0392
27	28	.0080	.0392	32	.0080	.0392
28	29	.0080	.0392	33	.0080	.0392
29	30	.0080	.0392	34	.0080	.0392
30	0			35	.0236	.0392
31	32	.0080	.0392			

```
 32    33 .0080 .0392 36 .0080 .0392
 33    34 .0080 .0392 37 .0080 .0392
 34    35 .0080 .0392 38 .0080 .0392
 35     0             39 .0236 .0392
 36    37 .0080 .0392
 37    38 .0080 .0392 40 .0080 .0392
 38    39 .0080 .0392 41 .0080 .0392
 39     0             42 .0236 .0392
 40    41 .0080 .0392
 41    42 .0080 .0392 43 .0080 .0392
 42     0             44 .0236 .0392
 43    44 .0080 .0392
 44     0             45 .0236 .0392
 45     0
  0     0
$8 NRN IDFUEL LR(L) PHI(L)
  1     1     0 .2500  0 .2500  0 .2500  1 .1250
  2     1     0 .2500  0 .2500  1 .2500  2 .2500
  3     1     0 .2500  0 .2500  2 .2500  3 .2500
  4     1     0 .2500  0 .2500  3 .2500  4 .2500
  5     1     0 .2500  0 .2500  4 .2500  5 .2500
  6     1     0 .2500  0 .2500  5 .2500  6 .2500
  7     1     0 .2500  0 .2500  6 .2500  7 .2500
  8     1     0 .2500  0 .2500  7 .2500  8 .2500
  9     1     0 .2500  0 .2500  8 .2500  9 .2500
 10     1     1 .1250  2 .2500 10 .1250  0 .2500
 11     1     2 .2500  3 .2500 10 .2500 11 .2500
 12     1     3 .2500  4 .2500 11 .2500 12 .2500
 13     1     4 .2500  5 .2500 12 .2500 13 .2500
 14     1     5 .2500  6 .2500 13 .2500 14 .2500
 15     1     6 .2500  7 .2500 14 .2500 15 .2500
 16     1     7 .2500  8 .2500 15 .2500 16 .2500
 17     1     8 .2500  9 .2500 16 .2500 17 .2500
 18     1    10 .1250 11 .2500  0 .2500 18 .1250
 19     1    11 .2500 12 .2500 18 .2500 19 .2500
```

```
 20     1    12 .2500 13 .2500 19 .2500 20 .2500
 21     1    13 .2500 14 .2500 20 .2500 21 .2500
 22     1    14 .2500 15 .2500 21 .2500 22 .2500
 23     1    15 .2500 16 .2500 22 .2500 23 .2500
 24     1    16 .2500 17 .2500 23 .2500 24 .2500
 25     1    18 .1250 19 .2500  0 .2500 25 .1250
 26     1    19 .2500 20 .2500 25 .2500 26 .2500
 27     1    20 .2500 21 .2500 26 .2500 27 .2500
 28     1    21 .2500 22 .2500 27 .2500 28 .2500
 29     1    22 .2500 23 .2500 28 .2500 29 .2500
 30     1    23 .2500 24 .2500 29 .2500 30 .2500
 31     1    25 .1250 26 .2500  0 .2500 31 .1250
 32     1    26 .2500 27 .2500 31 .2500 32 .2500
 33     1    27 .2500 28 .2500 32 .2500 33 .2500
 34     1    28 .2500 29 .2500 33 .2500 34 .2500
 35     1    29 .2500 30 .2500 34 .2500 35 .2500
 36     1    31 .1250 32 .2500  0 .2500 36 .1250
 37     1    32 .2500 33 .2500 36 .2500 37 .2500
 38     1    33 .2500 34 .2500 37 .2500 38 .2500
 39     1    34 .2500 35 .2500 38 .2500 39 .2500
 40     1    36 .1250 37 .2500  0 .2500 40 .1250
 41     1    37 .2500 38 .2500 40 .2500 41 .2500
 42     1    38 .2500 39 .2500 41 .2500 42 .2500
 43     1    40 .1250 41 .2500  0 .2500 43 .1250
 44     1    41 .2500 42 .2500 43 .2500 44 .2500
 45     1    43 .1250 44 .2500  0 .2500 45 .1250
000
$10A N FRAC   CHAR         CHPW        CHPH
    1 1.000 7.71132E-04 9.79140E-02 9.79140E-02
    1 0.500 7.71132E-04 9.79140E-02 9.79140E-02
$10C JB(L)
    1    10    18    25    31    36    40    43     0
    1 1.000 1.15259E-03 8.81240E-02 4.89570E-02
    9    17    24    30    35    39    42    44     0
    1 0.5   1.34332E-03 1.02813E-01 2.44785E-02
```

```
   45     0
$12A DFUEL   TCLAD        RFUEL     RCLAD       DROD
  0.029167   8.33     -4   642.0     405.0       0.031167
$12B KFUEL    CFUEL        KCLAD     CCLAD       HGAP
   2.0       0.058         8.80      0.058       1000.
$14 N1    N2     N3    N4    N5    N6    N7    N8   NHTC  ISAT
    3     0     1     1     0     1     1     0     1     0
$15 ABETA BBETA NBBC GK
.03480 -0.10     0   0.0
$18 J4
    2
$20  J2    J3   JSLIP
    3     3
$22 IBC1  IBC2  IBC3  IBC4  IBC5  IBC6
    0     0     0     0     0     0
$26A KIJ FTM   SL   THETA
  0.5   0.0   0.5   0.0
$26B NCHF NCWC NUFC CGRID  NCPR  NTCPR RGE   FPRC SPACNG
    3     0     0  0.0     0     0   0.    0.    0.
$27ITRY NTRY FERROR WERRX DAMPP DAMPF HTCERR TERR ITRNSX ERRCON EPSP ISCHEM
    0     0   0.    0.    0.    0.  -.01    0.     0    0.    0.     1
$29 IH  HIN   GIN  PEXIT   DPS    IPS FNORM   CQ  GINBP BORIN  CQIN  HOUT
    0  559. 2.554 2163.   0.0     0   1.0    0.     0 1600.     0    0.
$30A TTIME NDT  NSLUG
   0.     0     0
$32 NP               NQ    NBOR
    0     0     0     0     0
$36 NSKIPX NSKIPT NOUT NPCHAN NPROD NPNODE NPLOT
    0     0     3     0     0     0     0
$37 Channel IDs to be printed         (i=1, NPCHAN)
$     1     9    26    35
$38 Rod IDs to be printed (i=1, NPROD)
$     1     6     9    24    32    36
$EOD
```

Appendix C: CFX Inputs

Table C-1. Table of inputs into the CFX-Pre workspace

Water Domain	Basic Settings	Fluid1	Option	Material Library
			Material	waternuke or water 1
		Morphology	Continuous Fluid	
		Reference Pressure	system pressure for specific geometry	
		Buoyancy Model	Option	Buoyant
			Buoy. Ref. Density	Expected bundle averaged density
			Ref Location	Cartesian Coordinates
				Inlet of bundle (0,0,0)
	Fluid Models	Heat Transfer	Option	Total Energy or Isothermal
			Fluid Temperature (only isothermal)	Temperature for specific geometry
		Turbulence	Option	k-Epsilon
			Wall Function	Scalable
Inlet BC	Basic Settings	Boundary Type	Inlet	
	Boundary Details	Mass and Momentum	Option	Normal Speed
			Normal Speed	Average Inlet Velocity
		Turbulence	Option	Medium (intensity=5%)

Table C-1. Continued

Inlet BC	Basic Settings	Boundary Type	Inlet	
	Boundary Details	Mass and Momentum	Option	Normal Speed
			Normal Speed	Average Inlet Velocity
		Turbulence	Option	Medium (intensity=5%)
Outlet BC	Basic Settings	Boundary Type	Outlet	
	Boundary Details	Mass and Momentum	Option	Average Static Pressure
			Relative Pressure	0
			Pres. Profile Blend	0.05 (default)
		Pressure Averaging	Option	Average Over Whole Outlet
Outer Wall BC	Basic Settings	Boundary Type	Wall	
	Boundary Details	Mass and Momentum	Option	No Slip Wall
		Wall Roughness	Option	Smooth Wall
Symmetry BC	Basic Settings	Boundary Type	Symmetry	
Rod Wall BC	Basic Settings	Boundary Type	Wall	
	Boundary Details	Mass and Momentum	Option	No Slip Wall
		Wall Roughness	Smooth Wall	
		Heat Transfer (if applicable)	Option	Heat Flux
			Heat Flux In	Specified Heat Flux at the location

CFX was set up using the ANSYS 13 Workbench. A CCL file was used to specify the material library. It communicated the range of temperatures and pressures to build a table using the International Association for the Properties of Water and Steam (IAPWS) database.

C.1 Material Definitions found within the CCL file

```
MATERIAL: WaterNuke
   Option = Pure Substance
   Thermodynamic State = Liquid
   Material Description = Liquid water, IAPWS EOS (339 K->623 K, \
                    30 bar -> 210 bar)
   Material Group = Water Data, IAPWS IF97
   PROPERTIES:
     Option = IAPWS Library
     REFERENCE STATE:
       Option = Automatic
     END
     TABLE GENERATION:
          Minimum Temperature = 339.00 [K]
          Maximum Temperature = 623.15 [K]
       Minimum Absolute Pressure = 30 [bar]
       Maximum Absolute Pressure = 210 [bar]
     END
   END
  END

MATERIAL: Water1
   Option = Pure Substance
   Thermodynamic State = Liquid
   Material Description = Liquid water, IAPWS EOS (273 K->623 K, \
                    0.01 bar -> 100 bar)
   Material Group = Water Data, IAPWS IF97
   PROPERTIES:
```

```
    Option = IAPWS Library
    REFERENCE STATE:
      Option = Automatic
    END
    TABLE GENERATION:
        Minimum Temperature = 273.15 [K]
        Maximum Temperature = 623.15 [K]
      Minimum Absolute Pressure = 0.01 [bar]
      Maximum Absolute Pressure = 100 [bar]
    END
  END
END
```

Appendix D: Table of Fluid Properties

Table D-1. Bundle averaged fluid properties at the inlet and exit of each bundle

	4x4		5x5		2x2		17x17	
	Inlet	Exit	Inlet	Exit	Inlet	Exit	Inlet	Exit
Pressure (psia)	1200.38	1197.98	1501.79	1497.79	16.116	11.146	2168.21	2157.84
Temperature (F)	201.176	336.863	351.09	378.058	77.000	77.000	559.558	595.695
Enthalpy (BTU/lbm)	171.978	310.003	325.065	353.439	45.115	45.102	558.911	607.364
Density (lbm/ft^3)	60.3257	56.3128	55.933	54.905	62.244	62.243	46.1746	43.4197
Viscosity (lbm/ft-hr)	0.7326	0.3964	0.375	0.346	5.98E-04	5.98E-04	0.2203	0.201
Specific Heat (BTU/lb-F)	1.0011	1.0378	1.04	1.055	0.999	0.999	1.2698	1.4123
Thermal Conductivity (BTU/hr-ft-F)	0.3937	0.3938	0.394	0.39	9.75E-05	9.75E-05	0.3318	0.3089